Acta Materialia 289 (2025) 120893

Contents lists available at ScienceDirect

Acta Materialia

journal homepage: www.elsevier.com/locate/actamat

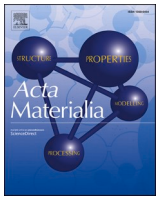

Mechanistic insights and kinetics of continuous and geometric dynamic recrystallisation in hot deformed aluminium alloy

Ruiqiang Zhang [a], Jieming S. Zhang [b], Wei Wang [a], Yuanbo T. Tang [b,c], Jun Jiang [a,*], Roger C. Reed [b,d], Jianguo Lin [a]

[a] Department of Mechanical Engineering, Imperial College London, London SW7 2AZ, UK
[b] Department of Materials, University of Oxford, Parks Road, Oxford, OX1 3PH, UK
[c] School of Metallurgy and Materials, University of Birmingham, Edgbaston, Birmingham, B15 2TT, UK
[d] Department of Engineering Science, University of Oxford, Parks Road, Oxford, OX1 3PJ, UK

ARTICLE INFO

Keywords:
Continuous dynamic recrystallisation
Geometric dynamic recrystallisation
Dynamic recovery
Grain boundaries
Hot compression
Aluminium alloy

ABSTRACT

Dynamic recrystallisation (DRX) is a significant restoration mechanism in the hot deformation of materials with high stacking fault energy (SFE), such as aluminium alloys. Both continuous DRX (CDRX) and geometric DRX (GDRX) have been observed concurrently during hot deformation of aluminium alloys. However, the kinetics of these DRX mechanisms during hot deformation remain considerably controversial in the literature, leading to the development of distinct constitutive models for CDRX and GDRX. To address this knowledge gap, the present study conducted hot compression tests on an aluminium alloy (AA6061) at varying strain levels up to 1.5. Crystallographic orientation and misorientation were characterised over a large area of the deformed samples using high-resolution electron backscatter diffraction (HR-EBSD) with a misorientation resolution of 0.05°. A quantitative analysis was then performed on the characteristics of high-angle grain boundaries (HAGBs), low-angle grain boundaries (LAGBs) and geometrically necessary dislocations (GNDs). The results indicate that CDRX initiates in the early stages of deformation and reaches saturation as deformation progresses. This saturation of CDRX is attributed to a reduction in GNDs and LAGBs. GDRX occurs slightly before CDRX saturation, then accelerates as deformation continues, ultimately becoming the dominant mechanism at higher strain levels. In addition, hot deformation results in formation of Σ3 (60° ⟨111⟩) twin boundaries (TBs), initially in the original HAGBs and subsequently in new HAGBs produced through GDRX. In contrast, these TBs are not observed in the new HAGBs generated through CDRX. This research provides significant insights into the kinetics of CDRX and GDRX in high SFE materials, supporting the development of predictive models for these DRX mechanisms.

1. Introduction

Metallic materials with high stacking fault energy (SFE), such as aluminium, are extensively used across a wide range of industries [1]. Their high SFE directly influences their deformation mechanisms and mechanical properties in various applications [2]. During hot deformation of high SFE materials, dynamic recovery (DRV) and dynamic recrystallisation (DRX) are main thermally activated restoration mechanisms which determine the final microstructure and properties of hot-formed products [3]. DRV involves the annihilation of dislocations with opposite Burgers vectors and rearrangement of dislocations into cell-like structures, eventually into equiaxed subgrain structures surrounded by low-angle grain boundaries (LAGBs) [4]. DRV is driven by two key mechanisms including the climb of the edge dislocations and the cross-slip of screw dislocations [5]. In high SFE materials such as aluminium, both climb and cross-slip mechanisms are particularly prevalent and activated, resulting in high DRV during hot deformation processes. Additionally, DRV is recognised for establishing the conditions required for the initiation of DRX, a sequential and complementary mechanism that often initiates under similar thermomechanical conditions.

DRX involves both formation and migration of HAGBs, typically occurring at elevated temperatures [6]. There are three popular types of DRX: discontinuous DRX (DDRX), continuous DRX (CDRX) and geometric DRX (GDRX) [7–9]. However, their occurrence in high SFE materials has been significantly controversial. DDRX occurs through the nucleation and growth of new grains, similarly to static recrystallisation

* Corresponding author.
E-mail address: jun.jiang@imperial.ac.uk (J. Jiang).

https://doi.org/10.1016/j.actamat.2025.120893
Received 5 December 2024; Received in revised form 7 February 2025; Accepted 2 March 2025
Available online 3 March 2025

Abbreviations

(SFE)	stacking fault energy
(DDRX)	discontinuous dynamic recrystallisation
(CDRX)	continuous dynamic recrystallisation
(GDRX)	geometric dynamic recrystallisation
(DRV)	dynamic recovery
(HAGB)	high-angle grain boundary
(LAGB)	low-angle grain boundary
(GND)	geometrically necessary dislocation
(HR-EBSD)	high-resolution electron backscatter diffraction
(SRX)	static recrystallisation
(IPF)	inverse pole figure
(TB)	twin boundary
(CSL)	coincidence site lattice
(GBE)	grain boundary engineering
(HCP)	hexagonal close-packed
(BCC)	body-centred cubic
(FCC)	face-centred cubic

(SRX). It is generally not expected in high SFE materials, primarily because the high SFE facilitates rapid DRV which effectively lowers dislocation density and reduces the driving force required for DDRX. However, the occurrence of DDRX has been widely reported in aluminium alloys including AA1xxx [10], AA2xxx [11], AA6xxx [12], and AA7xxx [13,14]. CDRX generates HAGBs through the gradual transformation of LAGBs, driven by the progressive accumulation of dislocations within these boundaries [15]. This mechanism has been widely reported in aluminium alloys, such as AA1xxx [10,16], AA2xxx [17], AA5xxx [16], AA6xxx [18,19], and AA7xxx [20]. However, the concept of CDRX was challenged in Refs. [21,22], where it was argued that DRV is a sufficient restoration mechanism in hot deformation of aluminium alloys. Additionally, GDRX occurs when grains thin to less than three subgrain diameters, leading to the contact and pinch-off of serrated HAGBs [23–26]. The occurrence of GDRX has been reported during hot deformation of aluminium alloys, such as AA1xxx [10], AA2xxx [27], AA6xxx [28], and AA7xxx [29].

A recent study by some of the present authors [30] demonstrated that both CDRX and GDRX concurrently occur during hot deformation of an aluminium alloy AA6061, whereas DDRX is absent due to the rapid occurrence of DRV. This study showed that CDRX produces discontinuous or discrete HAGBs, while GDRX results in the formation of fine, equiaxed grains. However, the evolution of CDRX and GDRX mechanisms in high SFE materials such as aluminium alloys during their hot deformation remains significantly controversial. It has been reported that CDRX dominates at relatively low strain levels [14,16,31], while GDRX occurs at higher strain levels [21,24,32]. However, a conflicting claim was made in Refs. [33–36], stating that CDRX dominates at severe deformation. These varying experimental observations lead to the development of distinct constitutive models for CDRX. An early CDRX model proposed in Ref. [15] predicts that CDRX appears at a strain of 0.9 and saturates at a strain of 5 in AA1200 at 460 °C and 0.01 s^{-1}. This model also suggests that the saturation of CDRX is accompanied by saturation in the density of LAGBs as the microstructure approaches a steady state at large strains. In contrast, more recent CDRX models developed in Refs. [20,37–39] predict that CDRX begins at the very onset of deformation and then increases at a progressively decreasing rate. Additionally, an alternative model presented in Ref. [40] suggests that, with increasing strain, CDRX accelerates, growing at an increasing rate as deformation progresses.

These controversial observations are primarily attributed to the challenges in accurately differentiating HAGBs generated through different DRX mechanisms [41,42]. Some studies have reported that CDRX produces discrete segments of HAGBs [16,30], while others suggest that CDRX leads to the formation of fine grains fully enclosed by HAGBs [13,43]. Additionally, some studies indicate that CDRX can result in both types of HAGBs, producing a combination of discrete boundary segments and fully developed HAGBs around fine grains [20,37]. It is widely accepted that GDRX produces fine equiaxed grains [8,26,44]; however, the differences between these grains and those generated through CDRX or DDRX remain poorly understood. In fact, GDRX has even been considered as a subtype of CDRX in some studies [3].

The other challenges leading to the controversial observations result from the limitations of electron backscatter diffraction (EBSD) characterisation techniques and the complexity of quantitative data post-processing [45,46]. Until recently, a statistically representative high-resolution EBSD (HR-EBSD) method was unavailable for systematically investigating the effects of strain, strain rate, and temperature on the underlying DRX mechanisms [47]. Advances in scanning technology have increased speeds from approximately 100 points per second (PPS) at an angular resolution of 0.5° to over 3000 PPS with similar sensitivity [47], enabling the capture of statistically meaningful microstructure maps within a reasonable timeframe. Furthermore, recent advancements in tools such as the MATLAB toolbox and specialised EBSD post-processing software have enabled more robust and efficient statistical analyses [48]. Coupled with Gleeble thermal-mechanical systems [49], which allow systematic studies through precise variation of strain, strain rate, and temperature, these advancements make it possible to address the long-standing ambiguities surrounding the elusive DRX mechanisms in high SFE materials. Using these techniques, the present authors recently demonstrated concurrent occurrence of CDRX and GDRX during the hot deformation of an aluminium alloy [30]. This finding provides opportunities to further explore their evolution in high SFE materials during the hot deformation.

HAGBs are commonly classified using the coincidence site lattice (CSL) model. Each boundary is assigned a sigma (Σ) value, representing the reciprocal of the density of lattice sites shared by both crystals. According to the CSL model, special grain boundaries are characterised by low Σ values, typically in the range of $1 < \Sigma < 29$, while random boundaries are defined as those with $\Sigma \geq 29$ [50]. Σ3 grain boundaries, commonly referred to as Σ3 twin boundaries (TBs), are representative low-Σ grain boundaries that are thermodynamically stable and exhibit lower energy compared to the random boundaries due to their higher degree of atomic coherence and periodicity. Σ3 TBs are frequently observed in face-centred cubic (FCC) metals and alloys with low-to-medium SFE, such as copper or stainless steel, where they are primarily generated through deformation twinning [51] or annealing twining [52,53]. Research has shown that Σ3 TBs can significantly enhance material properties, including creep strength, fatigue property, corrosion resistance, and radiation tolerance [54,55]. This leads to the development of grain boundary engineering (GBE) which focuses on increasing the fraction of special grain boundaries [56–58]. Σ3 TBs have also been observed in high SFE materials such as aluminium [59–64], although their formation is known to be challenging in such materials [65]. However, the formation of Σ3 TBs during hot deformation processes in high SFE materials, along with the associated characteristics and kinetics, has been rarely reported and remains poorly understood.

The present study aims to investigate the kinetics of CDRX and GDRX mechanisms during the hot compression of an aluminium alloy AA6061. A series of hot compression tests were carried out on AA6061 at varying strain levels. The resulting crystallographic microstructures were characterised over sufficiently large regions using HR-EBSD technology for quantitative analyses. The evolution of the characteristics of HAGBs, LAGBs, and GNDs was systematically analysed. Furthermore, the densities of HAGBs produced through CDRX and GDRX, as well as the density of Σ3 TBs, were quantified separately. This study will provide valuable insights into the underlying DRX mechanisms in high SFE materials and support the development of predictive models for these

processes.

2. Methodology

A cast and homogenised aluminium alloy AA6061 ingot, with chemical composition of Al-0.50Si-0.70Fe-0.25Cu-0.15Mn-1.0Mg-0.25Zn-0.09Cr-0.15Ti (wt.%), was used in this study. Cylindrical samples, with a diameter of 8 mm and length of 12 mm, were cut from the as-received ingot. As shown in Fig. 1(a), hot compression tests on these samples were carried out using a Gleeble system. During the testing, samples were heated using the direct resistance heating method at a heating rate of 1 °C/s to achieve the target deformation temperature. After soaking for 3 min at this target temperature, the samples were deformed at the target strain rate to a certain strain level. Subsequently, the samples were water cooled to room temperature within 1 s. A pair of K-type thermocouples was welded at the centre of the sample to monitor its temperature. Table 1 lists all testing temperatures, strain rates and strain levels adopted in this study. Each test condition was repeated at least twice.

The crystallographic microstructures of the samples after the hot compression tests were characterised using the HR-EBSD technology. For this purpose, the deformed cylindrical samples were cut along the axial direction from the centre, as shown in Fig. 1(a). The samples were firstly ground using Silicon Carbide (SiC) abrasive papers with grit sizes from P800 to P4000, followed by polishing using diamond suspensions with micron sizes from 3 to 1 μm. Subsequently, they were electro-polished in a solution of 10% perchloric acid and 90% ethanol by volume, at a voltage of 20 V for approximately 30 s. The polished samples were finally scanned using a scanning electron microscope (SEM) equipped with an Oxford Instruments AZtec EBSD system. The scans were conducted with a fixed step size of 2 μm, producing an EBSD map measuring 1800 μm × 700 μm for each sample. The EBSD data were processed using the MATLAB toolbox MTEX (Version 5.7.0). The half-quadratic filter in MTEX was applied to denoise the EBSD data, utilising the default smoothing parameters. Grain boundaries were categorised based on misorientation angles θ, with HAGBs defined as those with $\theta \geq 15°$, and LAGBs defined as those with $2° \leq \theta < 15°$. The density of grain boundaries was calculated by dividing their total length (unit: m) by the area (unit: m^2) of the observed region, leading to a unit of m^{-1}. The GND density, ρ, was estimated by calculating the curvature tensor of the crystalline lattice. This estimation included a linear optimisation step aimed at minimising the total energy, refining the GND density calculation [66].

Table 1
Deformation conditions for hot compression tests including temperatures T, strain rates $\dot{\varepsilon}$ and strain levels ε.

	$\varepsilon = 0.5$	$\varepsilon = 0.75$	$\varepsilon = 1$	$\varepsilon = 1.5$
$T = 400$ °C, $\dot{\varepsilon} = 0.1$ s^{-1}	√	√	√	√
$T = 475$ °C, $\dot{\varepsilon} = 0.1$ s^{-1}	√	√	√	√

Fig. 1(b1) and (b2) shows the inverse pole figure (IPF) map and the corresponding map of HAGBs and LAGBs for the as-received AA6061. The alloy reveals a relatively uniform grain size distribution across the observed region. Fig. 1(c) displays the corresponding pole figures for the crystal directions [100], [110] and [111], indicating a random texture in the as-received alloy [30].

3. Results

3.1. Evolution of characteristics of HAGBs and occurrence of DRX

The occurrence of DRX results in both the formation and migration of HAGBs. Fig. 2 presents the evolution of the HAGB distributions for the samples deformed to different strain levels $\varepsilon = 0.5$, 0.75, 1 and 1.5 at 400 °C & 0.1 s^{-1} (Fig. 2(a1)–(a4)) and 475 °C & 0.1 s^{-1} (Fig. 2(b1)–(b4)). The HAGBs comprise of continuous HAGBs (black lines) and discontinuous HAGBs (red lines). They are categorised based on their ability to form closed loops: continuous HAGBs form closed loops, while discontinuous or discrete HAGBs do not, similar to the method described in Ref. [30]. As seen, both continuous HAGBs and discontinuous HAGBs increase across the observed region as the deformation level rises. Notably, a great number of fine equiaxed grains were formed when the alloy was compressed to relatively high strain levels such as $\varepsilon = 1.5$ under both testing conditions. A previous study by some of the present authors [30] demonstrated that GDRX contributes to the formation of fine equiaxed grains, while CDRX results in the formation of discontinuous HAGBs. The following subsections will provide further evidence and analyse the kinetics of these DRX mechanisms during hot compression.

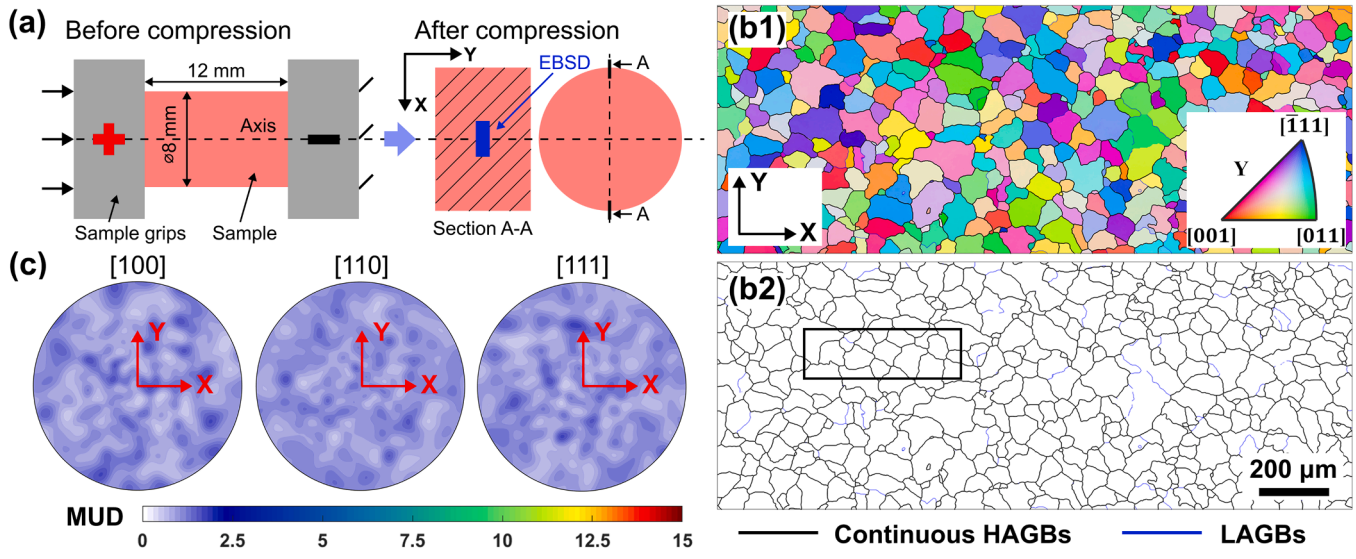

Fig. 1. Hot compression tests and initial microstructure of as-received AA6061, (a) Experimental setup for hot compression tests, including the size of sample and location for EBSD characterisation, with symbols '+' and '−' indicating positive and negative electrodes, respectively, for direct resistance heating, (b1) Inverse pole figure (IPF) map showing crystal orientations along the Y-axis (compression direction), (b2) Corresponding map showing all HAGBs and LAGBs, and (c) Pole figures for crystal directions [100], [110] and [111], showing the texture.

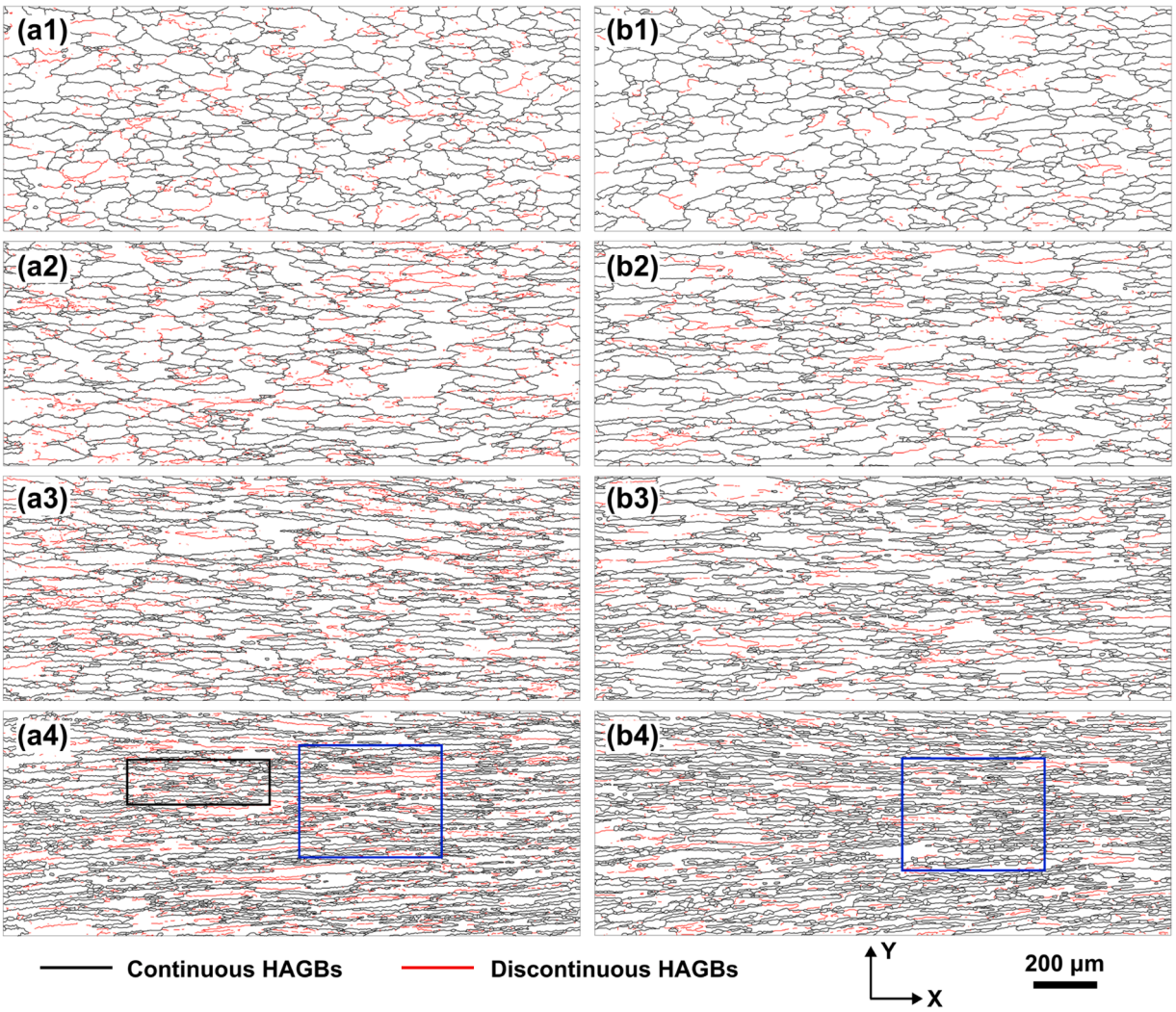

Fig. 2. Maps showing all HAGBs comprising continuous HAGBs (black lines) and discontinuous HAGBs (red lines) in AA6061 deformed during hot compression tests at different strain levels: (a1)–(b1) 0.5, (a2)–(b2) 0.75, (a3)–(b3) 1 and (a4)–(b4) 1.5. Additionally, (a1)–(a4) at 400 °C and 0.1 s^{-1} and (b1)–(b4) at 475 °C and 0.1 s^{-1}.

3.1.1. Continuous HAGBs and occurrence of GDRX

Fig. 3(a) and (b) shows the density of continuous HAGBs in AA6061 samples deformed at 400 °C & 0.1 s^{-1} and 475 °C & 0.1 s^{-1}, respectively. The microstructure data of the as-received alloy (Fig. 1) was used to represent zero deformation ($\varepsilon = 0$), as the alloy had been homogenised, as described in Section 2. As the deformation level rises, the continuous HAGB density increases, particularly when the deformation strain surpasses approximately 0.75. Fig. 3(c) and (d) displays the misorientation angle distributions of the continuous HAGBs. The continuous HAGBs in the as-received alloy ($\varepsilon = 0$) have misorientation angles ranging from 15° to 61°, and those with a misorientation angle of approximately 45° exhibit the highest density. As the alloy was deformed to $\varepsilon = 0.5$ or 0.75 under both testing conditions, only the continuous HAGB density with misorientation angles ranging from approximately 45° to 61° increases. When the alloy was further deformed to $\varepsilon = 1$ or 1.5 under both testing conditions, the continuous HAGB density with any misorientation angles ranging from 15° to 61° increases. This is particularly pronounced for the continuous HAGBs with misorientation angles around 59.5°, where their density at $\varepsilon = 1.5$ shows an increase of over 700% compared to the as-received alloy ($\varepsilon = 0$). Fig. 3(e) and (f) presents the number of grains against their perimeters at 400 °C & 0.1 s^{-1} and 475 °C & 0.1 s^{-1}, respectively. It should be noted that these grains are enclosed by continuous HAGBs. As the deformation progresses under both testing conditions, the number of grains with perimeters ranging from 15 to 200 μm increases significantly, particularly the grains with perimeters around 35 μm. For example, the number of grains with a perimeter of 35 μm is increased by over 3000% when deformed from $\varepsilon = 0$ to 1.5 at 400 °C & 0.1 s^{-1}. However, the number of the grains with perimeters exceeding 200 μm remains relatively unchanged. A previous study by some of the present authors [30] identified the fine equiaxed grains with perimeters of 200 μm and less, as the products due to the occurrence of GDRX. The resulting data presented in Fig. 3(e) and (f) further support this finding. It should be noted that this critical grain perimeter probably depends on deformation conditions, such as temperature and strain rate. However, for simplicity and consistency, a conservative value of 200 μm was adopted in the present study to identify fine equiaxed grains. Furthermore, at the same strain level $\varepsilon = 1$ or 1.5, higher deformation temperatures result in a lower number of grains.

Fig. 4(a) and (b) displays the density of continuous HAGBs of fine equiaxed grains with perimeters of 200 μm or less, in AA6061 samples deformed at different strain levels under conditions of 400 °C & 0.1 s^{-1} and 475 °C & 0.1 s^{-1}, respectively. The maps showing the fine grain distributions are presented in Appendix A. At a strain level of $\varepsilon = 0$, the continuous HAGB density is approximately 15 × 10^3 m^{-1}. This indicates that fine grains are present in the as-received alloy, which can also be seen in Fig. 3(e) and (f). As the deformation rises to $\varepsilon = 0.5$, the HAGB

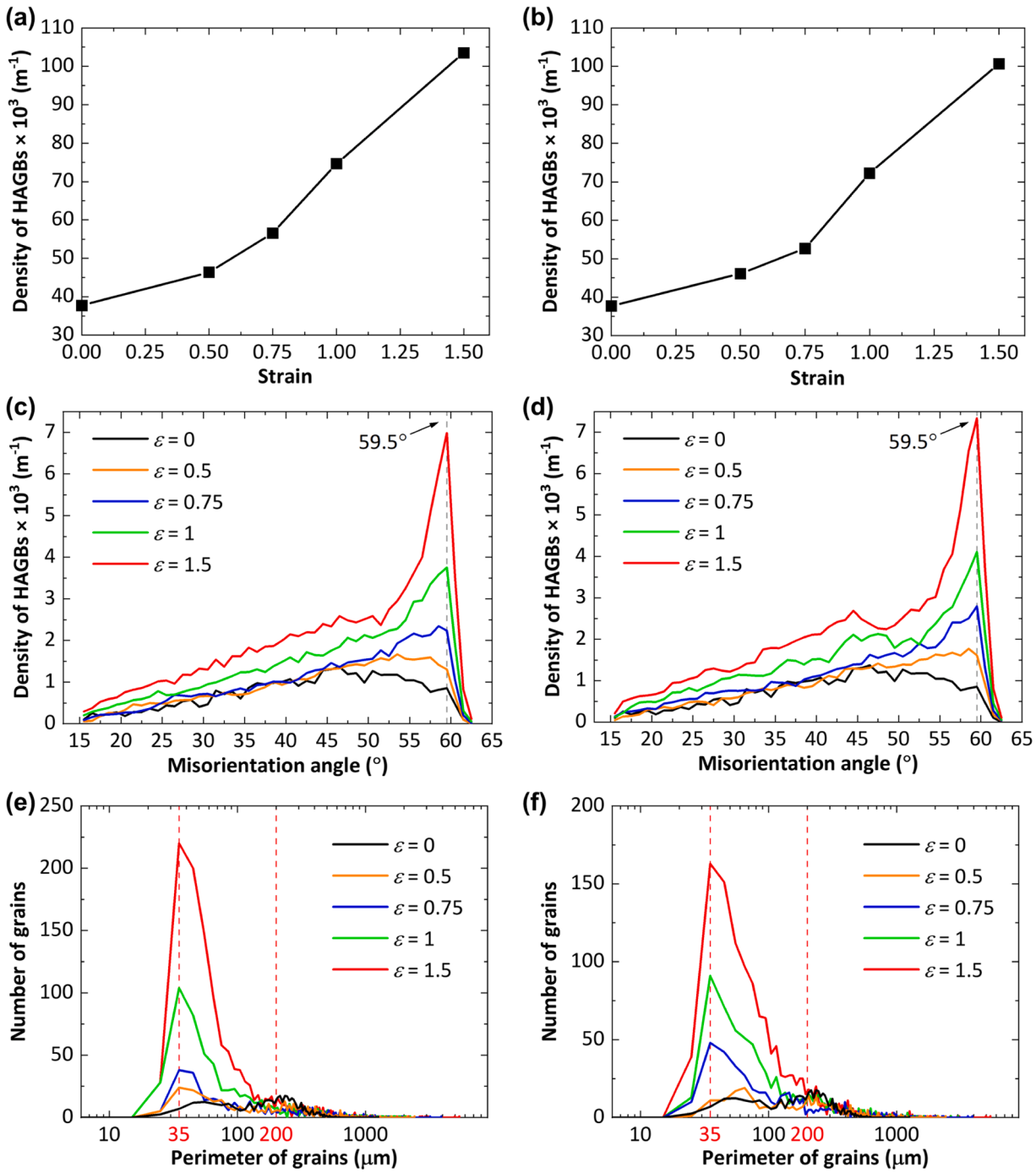

Fig. 3. Evolution of the characteristics of continuous HAGBs in AA6061 deformed during hot compression tests at different strain levels, (a) and (b) Density of continuous HAGBs, (c) and (d) Misorientation angle distributions of continuous HAGBs, (e) and (f) Number of grains as a function of their perimeter. Additionally, (a), (c), (e) at 400 °C and 0.1 s^{-1}, and (b), (d), (f) at 475 °C and 0.1 s^{-1}.

density almost remains unchanged, indicating that GDRX has not been initiated. When the deformation exceeds $\varepsilon = 0.75$, the HAGB density increases significantly, suggesting that GDRX occurs at higher strain levels. It is worth noting that GDRX occurs slightly earlier at 475 °C & 0.1 s^{-1} than at 400 °C & 0.1 s^{-1}. Fig. 4(c) and (d) shows the misorientation angle distributions for the continuous HAGBs surrounding the fine grains. These distributions exhibit similar shapes to those of all the continuous HAGBs displayed in Fig. 3(c) and (d). Furthermore, the increase in HAGB density results from the increase in HAGBs across a range of misorientation angles from 15° to 61°, which is particularly pronounced for HAGBs with misorientation angles around 59.5°.

3.1.2. Discontinuous HAGBs and occurrence of CDRX

Fig. 5(a) and (b) illustrates the density of discontinuous HAGBs in AA6061 samples deformed to different strain levels at 400 °C & 0.1 s^{-1} and 475 °C & 0.1 s^{-1}, respectively. At a strain level of $\varepsilon = 0$, the discontinuous HAGB density is zero. As deformation progresses, the discontinuous HAGB density rapidly increases and reaches saturation as the microstructure approaches a steady state. In a previous study by some of the present authors [30], it was demonstrated that these discontinuous HAGBs were produced due to the occurrence of CDRX. The rapid increase in the discontinuous HAGB density at the onset of hot deformation indicates the initiation of CDRX. Furthermore, CDRX is

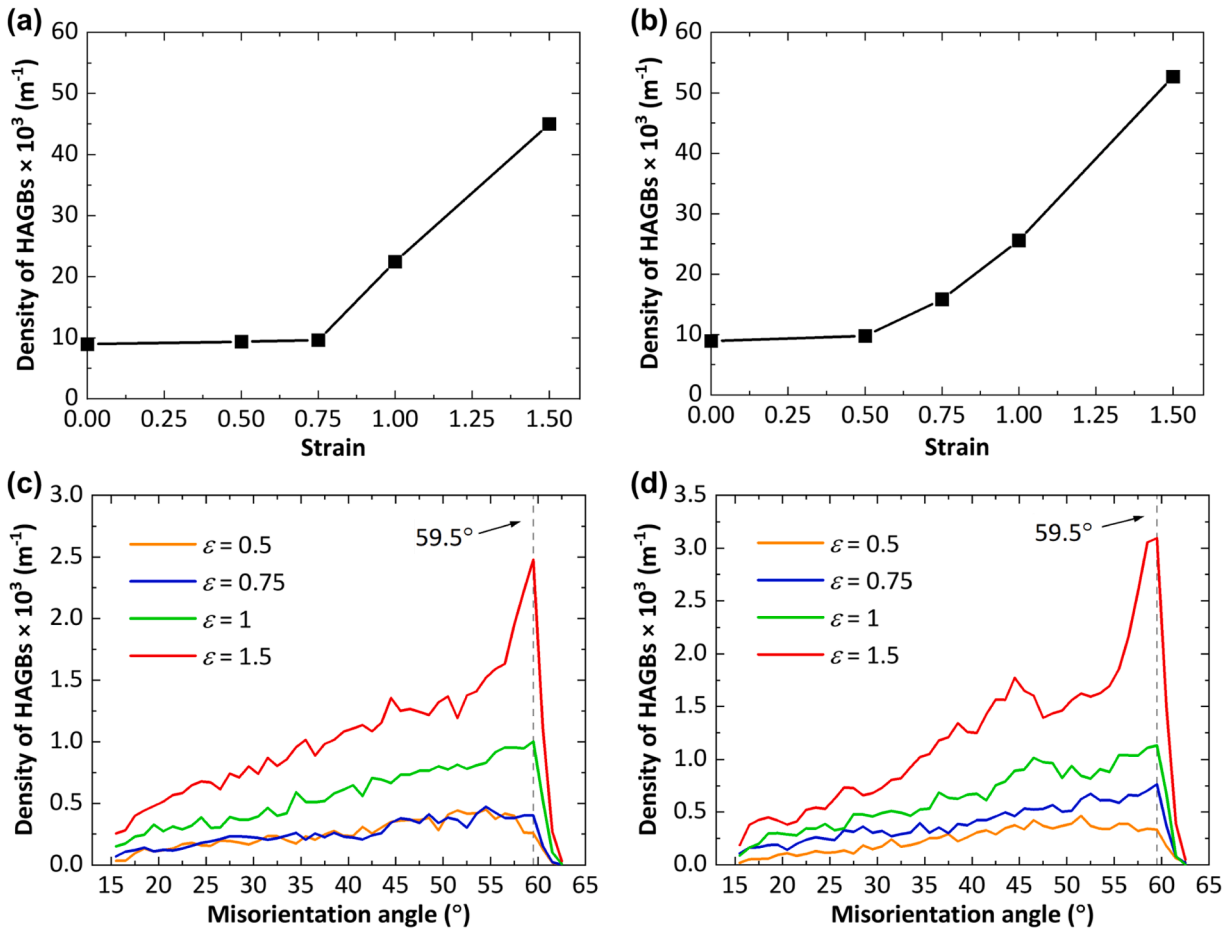

Fig. 4. Evolution of the characteristics of the selected continuous HAGBs of the fine grains with perimeters less than or equal to 200 μm, in AA6061 deformed during hot compression tests at different strain levels, (a) and (b) Density of continuous HAGBs, (c) and (d) Misorientation angle distributions of continuous HAGBs. Additionally, (a), (c) at 400 °C and 0.1 s^{-1}, and (b), (d) at 475 °C and 0.1 s^{-1}.

approaching completion at high strain levels as the density reaches saturated levels. Fig. 5(c) and (d) displays the misorientation angle distributions for the discontinuous HAGBs. Similarly to the observation reported in [30], these distributions differ significantly from the misorientation angle distributions of the continuous HAGBs, as presented in Fig. 3(c) and (d), although their misorientation angles also range from 15° to 61°. For the discontinuous HAGBs, their density reaches its highest values at a misorientation angle of 15°. As the misorientation angle increases, their density gradually decreases. Notably, the discontinuous HAGB density with misorientation angles above 40° is nearly zero. Furthermore, the increase in the total density of discontinuous HAGBs is primarily due to the increase in the discontinuous HAGBs with misorientation angles from 15° to approximately 35°, particularly those at a misorientation angle of 15°. When the discontinuous HAGB density reaches saturation at relatively high strain levels, their misorientation angle distribution remains unchanged.

3.1.3. Comparison of CDRX and GDRX

Fig. 6(a) and (b) presents a comparison of the density of continuous HAGBs surrounding fine equiaxed grains (perimeter ≤ 200 μm) produced through GDRX and discontinuous HAGBs formed through CDRX, at 400 °C & 0.1 s^{-1} and 475 °C & 0.1 s^{-1}, respectively. The density of continuous HAGBs through GDRX was adjusted by excluding the contribution from the fine grains in the as-received alloy. As observed, CDRX initiates early in the hot deformation process, with its intensity increasing as deformation progresses. When strain levels approach approximately $\varepsilon = 0.75$, CDRX reaches near completion. In contrast, GDRX begins at higher strain levels, around $\varepsilon = 0.75$ and accelerates as deformation progresses. With the completion of CDRX at higher strain levels, GDRX produces a higher density of HAGBs than CDRX and becomes the dominant DRX mechanism responsible for the formation of more HAGBs. Specifically, when deformed to $\varepsilon = 1.5$ at 475 °C & 0.1 s^{-1}, GDRX produces a HAGB density of 44.7 × 10^3 m^{-1}, which is approximately 300% higher than that produced through CDRX.

3.2. Evolution of characteristics of LAGBs and GNDs

While HAGBs play a key role in DRX, the evolution of LAGBs and GNDs within grains also significantly contributes to its occurrence. To further understand their effects on DRX kinetics, the characteristics of both LAGBs and GNDs were analysed. Fig. 7(a) and (b) shows the density of LAGBs and GNDs in AA6061 samples deformed at different strain levels under conditions of 400 °C & 0.1 s^{-1} and 475 °C & 0.1 s^{-1}, respectively. The corresponding distribution maps are provided in Appendix B. The density of LAGBs at the beginning of hot compression is nearly zero (Fig. 1(b1) and (b2)). As deformation progresses, the density accelerates and reaches a peak value at a strain level around $\varepsilon = 0.75$. With further deformation, however, the density of LAGBs gradually decreases. The evolution of the density of GNDs exhibits a similar trend. The GND density increases in the initial stage of deformation and reaches its peak value at $\varepsilon = 0.75$, while it begins to decrease with further deformation. Fig. 7(c) and (d) displays the misorientation angle distributions for LAGBs. The distributions at different strain levels show a similar trend that its density decreases as the misorientation angle increases from 2° to 15°. It is interesting to notice that the density of LAGBs with a misorientation angle of 15° increases progressively with

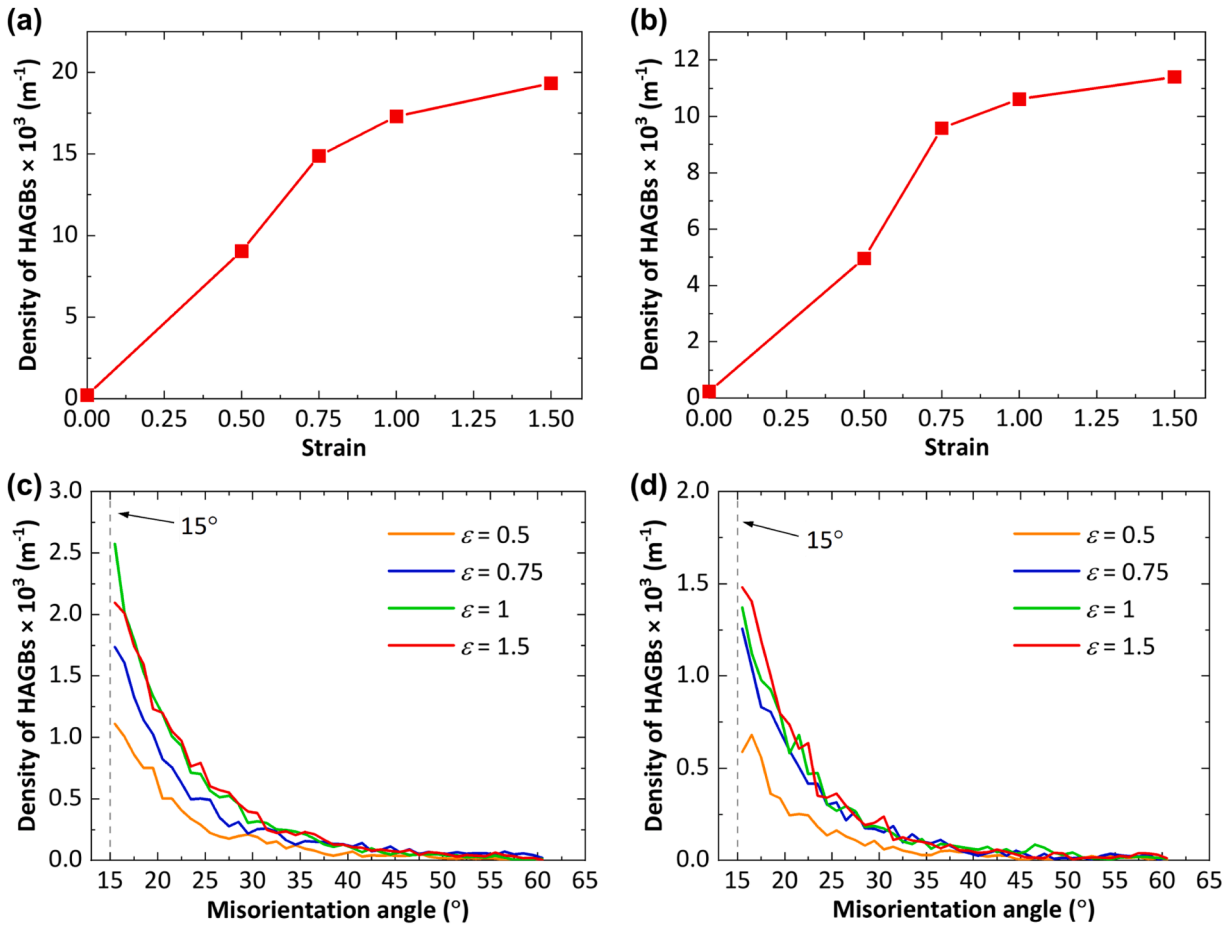

Fig. 5. Evolution of the characteristics of discontinuous HAGBs in AA6061 deformed during hot compression tests at different strain levels, (a) and (b) Density of discontinuous HAGBs, (c) and (d) Misorientation angle distributions of discontinuous HAGBs. Additionally, (a), (c) at 400 °C and 0.1 s^{-1}, and (b), (d) at 475 °C and 0.1 s^{-1}.

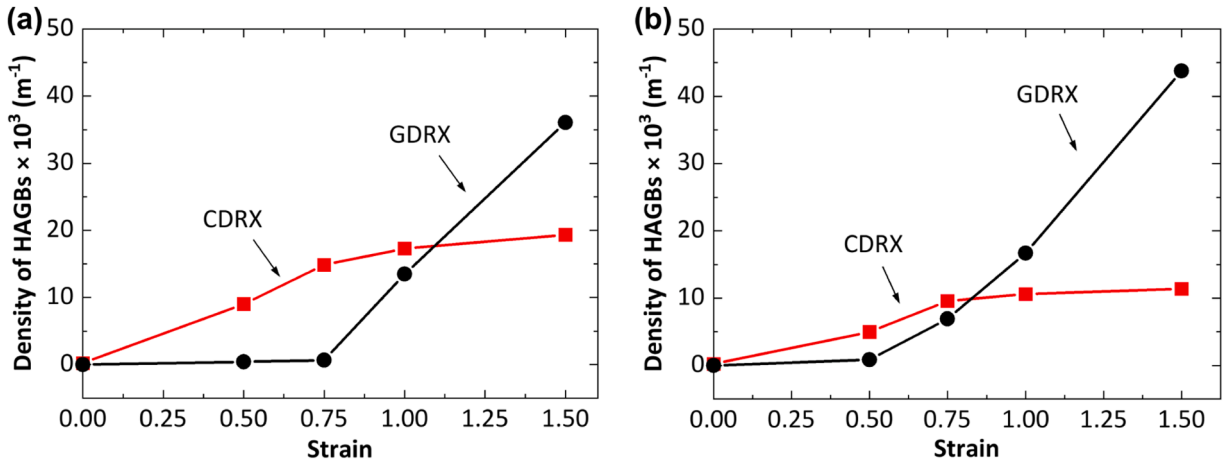

Fig. 6. Comparison of the density of continuous HAGBs of fine grains (perimeter ≤ 200 μm) produced through GDRX and discontinuous HAGBs produced through CDRX in AA6061 deformed during hot compression tests at different strain levels up to $\varepsilon = 1.5$ at (a) 400 °C and 0.1 s^{-1} and (b) 475 °C and 0.1 s^{-1}.

deformation, even though the total LAGB density initially rises and subsequently declines. This indicates a gradual transformation of LAGBs from lower to higher misorientation angles.

3.3. Evolution of local curvatures of HAGBs

Previous studies [24,26,44] have demonstrated that the serrations of HAGBs contribute to the occurrence of GDRX. However, quantitative evaluation of HAGB serrations remains challenging [67]. In the present study, the local curvature of HAGBs was calculated by fitting circles to local grain boundaries and taking the reciprocal of their radius using the 'curvature' command in MTEX. Higher curvature values indirectly suggest greater HAGB serrations [30]. Fig. 8(a) shows the magnified regions in the as-received alloy and the alloy deformed to $\varepsilon = 1.5$ at 475

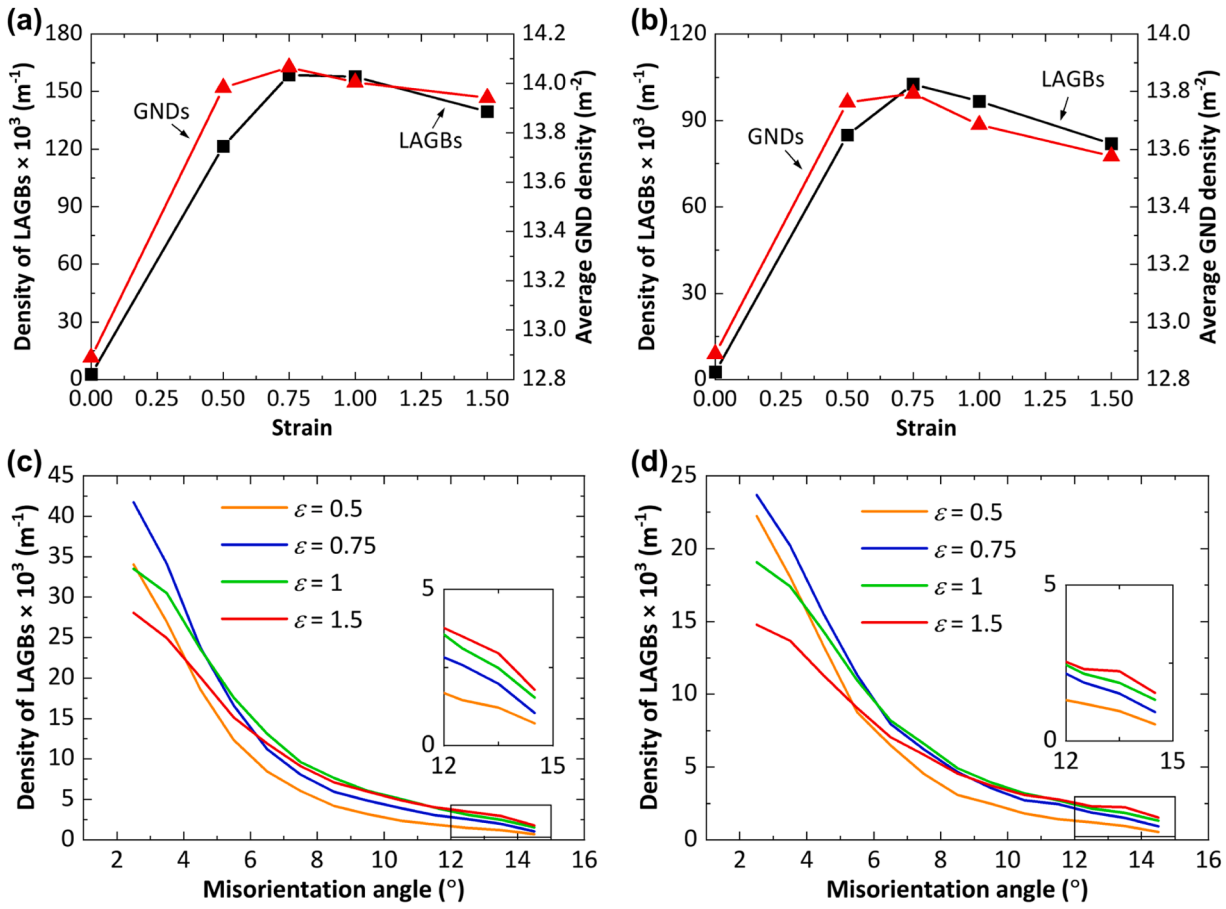

Fig. 7. Evolution of the characteristics of LAGBs and GNDs in AA6061 deformed during hot compression tests at different strain levels, (a) and (b) Density of LAGBs and GNDs, (c) and (d) Misorientation angle distributions of LAGBs. Additionally, (a), (c) at 400 °C and 0.1 s^{-1}, and (b), (d) at 475 °C and 0.1 s^{-1}.

°C & 0.1 s^{-1}; these magnified regions are illustrated in Figs. 1(b2) and 2 (a4). Compared to the as-received alloy, both continuous and discontinuous HAGBs become serrated after hot deformation. Fig. 8(b) displays the curvature of the corresponding HAGBs. As observed, higher curvature values correspond to higher serrations, which supports the use of curvature values to evaluate HAGB serrations. Fig. 8(c) and (d) presents the curvature value distributions for continuous HAGBs in AA6061 deformed to different strain levels at 400 °C & 0.1 s^{-1} and 475 °C & 0.1 s^{-1}, respectively. Compared to the as-received alloy, where the curvature values for continuous HAGBs range from 0 to 0.25, the curvature values after hot deformation increase to a range of 0 to 0.45. As deformation progresses, the range of continuous HAGB curvature values remains unchanged. However, the density of these boundaries increases, particularly for these with relatively low curvature values. Fig. 8(e) and (f) shows the curvature value distributions for discontinuous HAGBs. Similarly to continuous HAGBs, the curvature values for discontinuous HAGBs range from 0 to 0.45. The increase in their total density is attributed to the rise in discontinuous HAGBs with relatively low curvature values. The maps showing the local curvatures of all HAGBs are displayed in Appendix C.

3.4. Formation of ⟨110⟩ fibre texture along compression direction

During hot deformation of AA6061, texture typically develops, which may influence the DRX process. Fig. 9(a1)–(a4) and (b1)–(b4) shows the evolution of ⟨110⟩ texture in AA6061 samples deformed at different strain levels under conditions of 400 °C & 0.1 s^{-1} and 475 °C & 0.1 s^{-1}, respectively. The corresponding IPF maps are presented in Appendix D. The ⟨110⟩ fibre texture along the compression direction (i.e. the Y-axis) develops when the alloy is deformed to $\varepsilon = 0.5$. As deformation progresses, this texture becomes stronger. To quantify the intensity of the ⟨110⟩ texture, its highest density values are obtained from respective pole figures. Fig. 9(c) displays the results. As seen, the ⟨110⟩ fibre texture forms at $\varepsilon = 0.5$ and becomes stronger as deformation increases. As ε surpasses 0.75, the texture tends to saturate. This suggests that the texture was primarily formed in the early stages of deformation. The textures continue to increase as deformation processes, while its increasing rate gradually decreases.

3.5. Formation of Σ3 twin boundaries (TBs)

According to Fig. 3(c) and (d), the density of continuous HAGBs at high misorientation angles between 52° and 61° increases significantly as deformation progresses, particularly for those with a misorientation of approximately 59.5°. To further study the characteristics of these HAGBs, the evolution of their total density was obtained, as plotted in Fig. 10(a). The corresponding distribution maps of these HAGBs are provided in Appendix E. As seen, the density of the HAGBs increases as deformation progresses, rising by approximately 370% from $\varepsilon = 0$ to 1.5. It should be noted that under the two testing conditions of 400 °C & 0.1 s^{-1} and 475 °C & 0.1 s^{-1}, there is little difference between the density of HAGBs with high misorientation angles. Fig. 10(b1)–(b4) and (c1)–(c4) presents the distribution of misorientation axes for HAGBs with high misorientation angles from 52° to 61° with respect to the crystal coordinate system. As observed, these HAGBs with high misorientation angles exhibit a preferred misorientation axis which aligns with the crystal direction of ⟨111⟩. As deformation progresses, the density of these HAGBs with a ⟨111⟩ misorientation axis increases significantly,

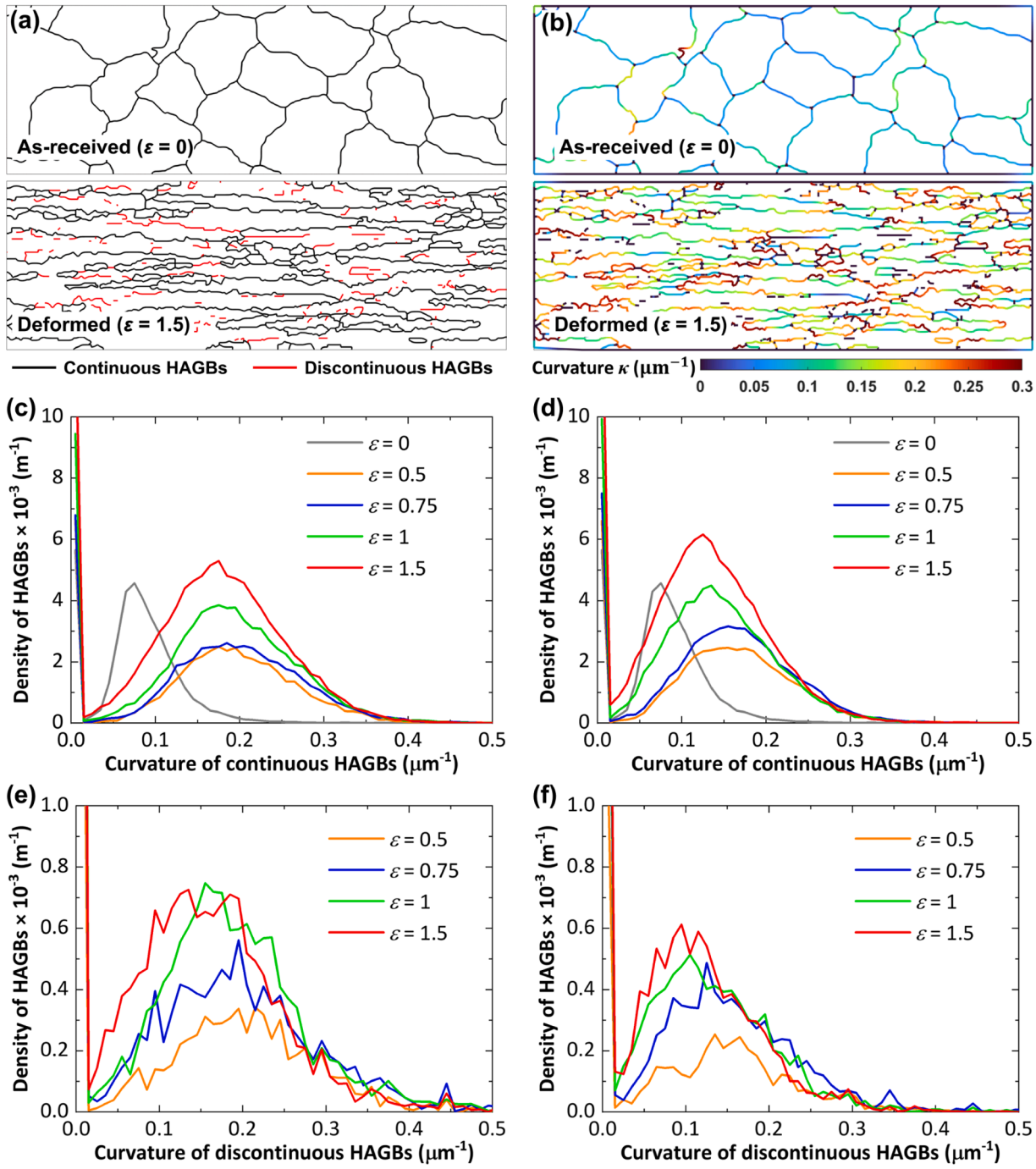

Fig. 8. Curvature values of HAGBs and their evolution in AA6061 deformed during hot compression tests at different strain levels, (a) Magnified regions of the HAGB maps in the as-received alloy (black rectangle in Fig. 1(b2)) and the alloy deformed to $\varepsilon = 1.5$ at 400 °C and 0.1 s^{-1} (black rectangle in Fig. 2(a4)), (b) Curvature of HAGBs in these magnified regions, (c) and (d) Curvature value distributions for continuous HAGBs, (e) and (f) Curvature value distributions for discontinuous HAGBs. Additionally, (c), (e) at 400 °C and 0.1 s^{-1}, and (d), (f) at 475 °C and 0.1 s^{-1}.

indicating the formation of abundant Σ3 TBs (60° ⟨111⟩) during deformation [64].

Fig. 11(a) and (b) displays the magnified regions within the IPF maps in AA6061 samples deformed to $\varepsilon = 1.5$ at 400 °C & 0.1 s^{-1} and 475 °C & 0.1 s^{-1}, respectively, highlighting the fine equiaxed grains in yellow colour, Σ3 TBs in the fine grains in green colour, and Σ3 TBs in the other HAGBs in blue colour. Considering that experimental measurements often show slight deviations from theoretical twin misorientations, all selected TBs in Fig. 11 exhibit a misorientation angle of 60° ± 5° and a misorientation axis within 5° of ⟨111⟩. It is worth noting that there is no Σ3 TBs formed in the discontinuous HAGBs. Furthermore, all these Σ3 TBs are not continuous, but discrete segments, similarly to the form of discontinuous HAGBs formed through CDRX. Fig. 11(c) and (d) plots Σ3 TBs in the fine equiaxed grains, Σ3 TBs in the other continuous HAGBs excluding those of the fine grains, and all Σ3 TBs, in AA6061 samples deformed at different strain levels under conditions of 400 °C & 0.1 s^{-1} and 475 °C & 0.1 s^{-1}, respectively. The corresponding distribution maps for these Σ3 TBs are presented in Appendix E. As seen, a few of Σ3 TBs exists in the as-received alloy ($\varepsilon = 0$), including in the fine grains and in the other continuous HAGBs. As the alloy is deformed to $\varepsilon = 0.5$, the density of Σ3 TBs in the fine grains remains unchanged, while the density of Σ3 TBs in the other continuous HAGBs increases. With further

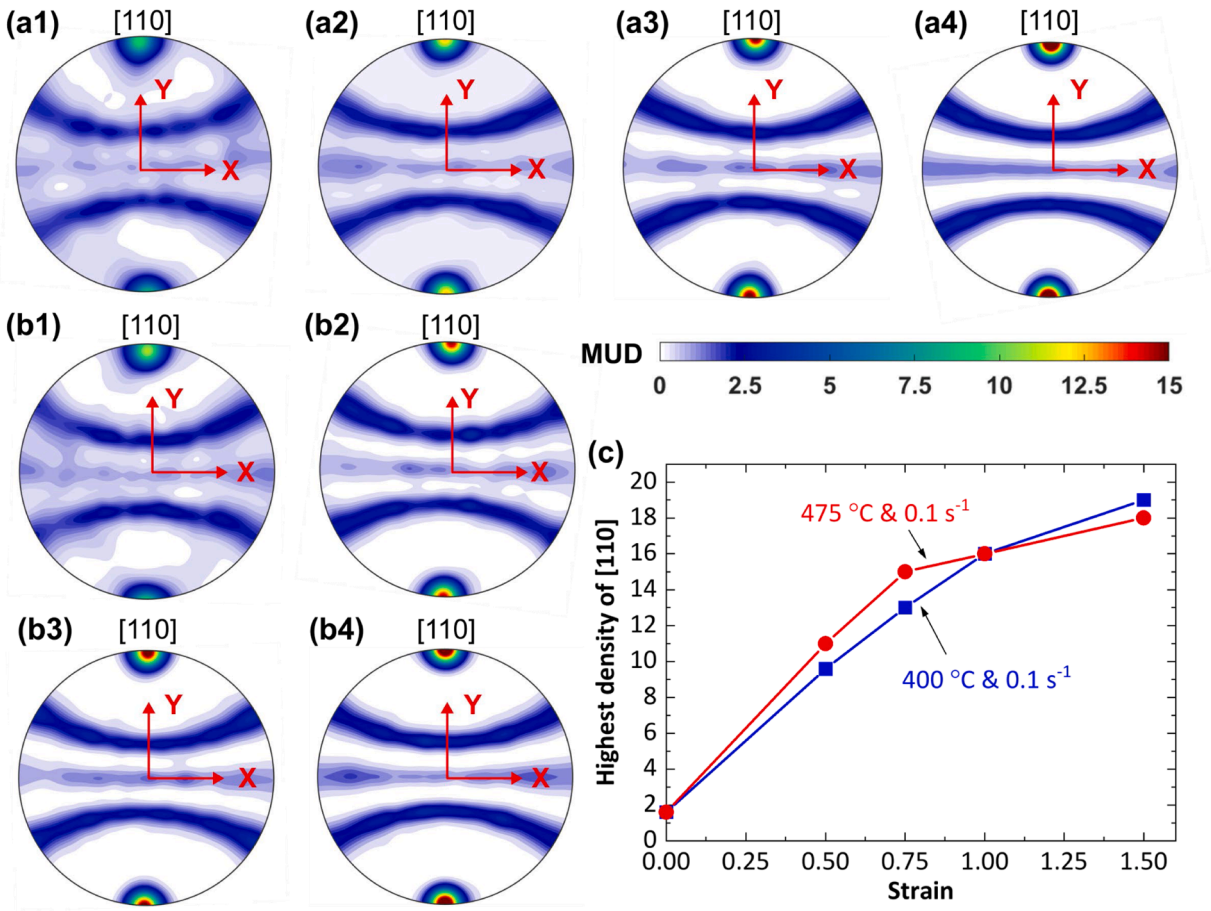

Fig. 9. ⟨110⟩ pole figures in AA6061 deformed during hot compression tests at different strain levels, (a1)–(b1) 0.5, (a2)–(b2) 0.75, (a3)–(b3) 1 and (a4)–(b4) 1.5. Additionally, (a1)–(a4) 400 °C and 0.1 s^{-1}, (b1)–(b4) at 475 °C and 0.1 s^{-1}. (c) Highest density of ⟨110⟩ at different strain levels.

deformation to $\varepsilon = 0.75$, the density of Σ3 TBs in the other continuous HAGBs continues to increase, while the density of Σ3 TBs in the fine grains at 400 °C & 0.1 s^{-1} remains unchanged and at 475 °C & 0.1 s^{-1} increases slightly. This indicates that the increase in Σ3 TBs of the fine grains is slightly delay than the increase in Σ3 TBs in the other continuous HAGBs. When the alloy is deformed to $\varepsilon = 1$ and 1.5, the density of both Σ3 TBs of the fine grains and in the other continuous HAGBs keeps increasing. These increases contribute to a continuing increase in the total density of all Σ3 TBs in AA6061 as deformation progresses. For example, the density of all Σ3 TBs is increased by approximately 620% with deformation from $\varepsilon = 0$ to 1.5 at 400 °C & 0.1 s^{-1}.

4. Discussion

4.1. Occurrence of CDRX and GDRX

Both continuous and discontinuous HAGBs were observed in hot deformed AA6061, as shown in Fig. 2. Their densities increase in different ways as the deformation progresses, as demonstrated in Figs. 3 (a) and (b) and 4(a) and (b). Additionally, the misorientation angle distributions of continuous and discontinuous HAGBs exhibit significantly different shapes, as illustrated in Figs. 4(c) and (d) and 5(c) and (d). A previous study performed by some of the present authors [30] demonstrated that during the hot compression of AA6061, CDRX results in the formation of discontinuous HAGBs while GDRX leads to the formation of fine equiaxed grains surrounded by continuous HAGBs. The present study provides more evidence to support these findings. Regarding CDRX, it involves a continuous process in which LAGBs transform into HAGBs by gradually increasing their misorientation angles [15,16]. As seen in Fig. 7(c) and (d), the misorientation angle distributions of LAGBs show a trend of gradually increasing their misorientation angles as deformation progresses. This trend is evidenced by a higher density of LAGBs at misorientation angles (θ) around 15° at higher deformation levels, although the total density of LAGBs firstly increases and subsequently decreases as shown in Fig. 7(a) and (b). Furthermore, the density of LAGBs at misorientation angles just below 15°, as shown in Fig. 7(c) and (d), is nearly equal to the density of discontinuous HAGBs at misorientation angles slightly above 15°, as displayed in Fig. 5(c) and (d). This further demonstrates the continuous transformation from LAGBs ($\theta < 15°$) into discontinuous HAGBs ($\theta \geq 15°$) due to CDRX. Additionally, the increase in the total density of discontinuous HAGBs is primarily attributed to the rising density of those with relatively low misorientation angles from 15° to 35°, particularly concentrated around 15°, as shown in Fig. 5(c) and (d). All these observations strongly support the occurrence of CDRX which produces discontinuous HAGBs.

A significant number of fine equiaxed grains were produced during the hot compression of AA6061, particularly at high compression strain levels such as $\varepsilon = 1$ and 1.5, as observed in Fig. 3(e) and (f). GDRX typically produces fine equiaxed grains as original grains become flattened and their HAGBs serrated under large strains, eventually allowing the boundaries to contact opposing sides or pinch off to form fine grains [24,25,44]. One may argue that these fine grains were probably produced due to the occurrence of DDRX, which typically involves the nucleation and growth of new grains [68]. However, this mechanism is unlikely because DDRX is generally not considered to occur in high SFE materials due to the rapid DRV. Furthermore, the previous study [30] demonstrated that the density of HAGBs of the fine grains is directly

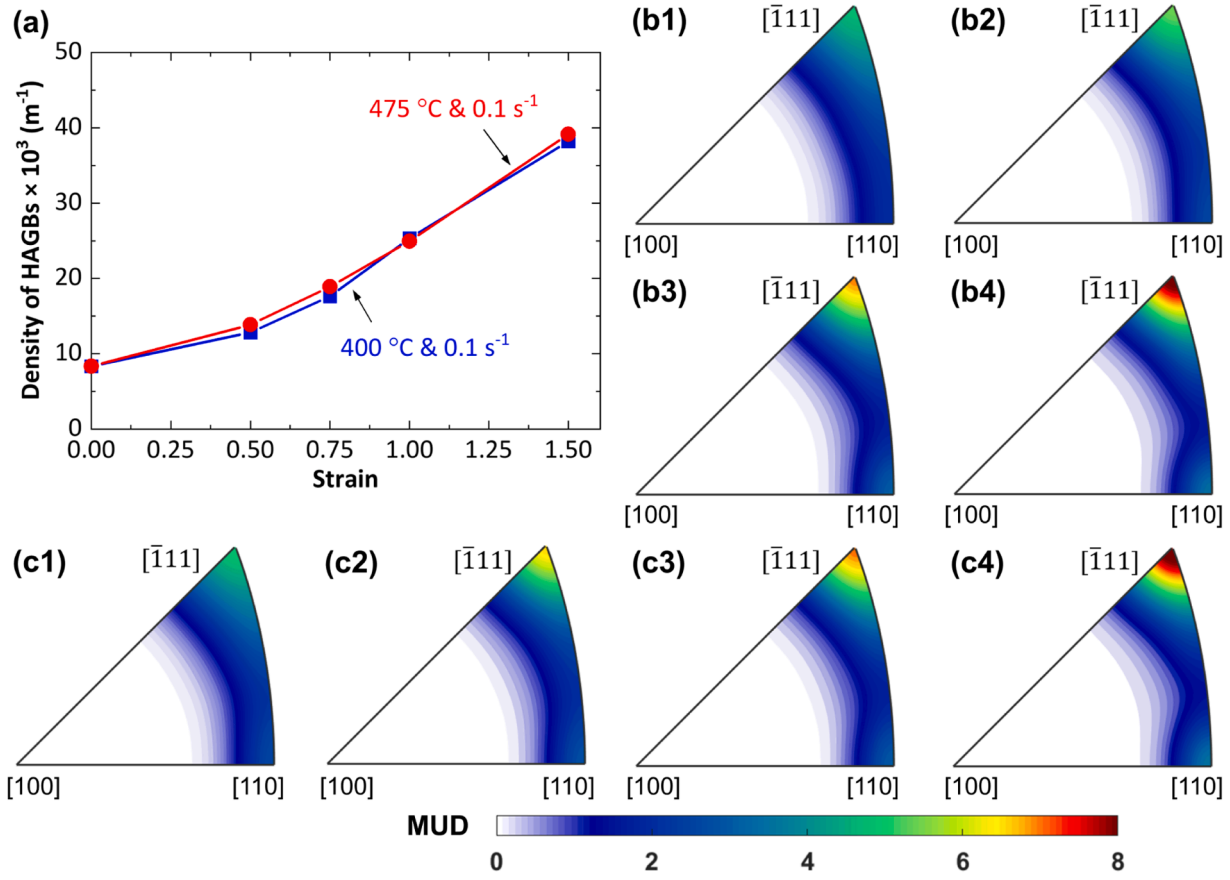

Fig. 10. (a) Density of all continuous HAGBs with misorientation angles ranging from 52° to 61° in AA6061 deformed during hot compression tests at different strain levels, (b1)–(b4) and (c1)–(c4) Misorientation axes of these HAGBs at different strain levels, (b1)–(c1) 0.5, (b2)–(c2) 0.75, (b3)–(c3) 1 and (b4)–(c4) 1.5. Additionally, (b1)–(b4) at 400 °C and 0.1 s^{-1}, and (c1)–(c4) at 475 °C and 0.1 s^{-1}.

proportional to the deformation temperature. This dependence contradicts the expected behaviour of DDRX, as higher temperatures further strengthen the rapid DRV in high SFE materials, which in turn suppresses DDRX activity [69]. Moreover, the misorientation angle distributions of the fine grains' HAGBs, as shown in Fig. 4(c) and (d), are very similar to those of the original HAGBs and those of all continuous HAGBs, as shown in Fig. 3(c) and (d). In addition, as observed in Fig. 8 (a)–(d), the continuous HAGBs exhibit significantly increased curvature values compared to those in the as-received alloy, suggesting their enhanced serrations as deformation progresses. This further indicates that the fine grains' HAGBs originate from the original continuous HAGBs through mechanisms of serration, contact and pinching off. Therefore, it can be concluded that these fine equiaxed grains were produced through GDRX.

It should be noted that the specimen shape significantly changes at large strains, such as $\varepsilon = 1.5$, which may serve as an additional indicator of GDRX occurrence, as GDRX occurs significantly at large strains, as shown in Fig. 2(a4) and (b4). Therefore, it may be inferred that GDRX can be distinguished from other DRX mechanisms based on the deformation mode, such as torsion. However, distinguishing between CDRX and GDRX based on test type may be challenging. GDRX occurs when materials undergo significant deformation, leading to a dramatic reduction in grain thickness to less than twice the size of subgrains [26, 44]. The term 'geometric' in GDRX primarily refers to the geometry of grains, rather than that of specimens [26,44]. In torsion, there are also opportunities to reduce grain thickness to meet this critical condition, suggesting that GDRX has the potential to occur in these types of tests as well. CDRX occurs through the progressive transformation of LAGBs into HAGBs, a process that is not directly influenced by grain geometry [15, 16]. As demonstrated in this manuscript, both CDRX and GDRX are observed in hot compression of AA6061.

4.2. *Kinetics of CDRX and GDRX*

As seen in Fig. 6, the density of discontinuous HAGBs produced through CDRX accelerates in the initial stages of hot deformation. As deformation progresses, the density reaches saturated levels. This suggests that CDRX initiates at the onset of hot deformation, leading to the accumulation of discontinuous HAGBs. When the deformation reaches certain levels, typically above $\varepsilon = 0.75$, as shown in Fig. 5(a) and (b), CDRX reaches completion and no more discontinuous HAGBs are produced, resulting in saturation in the total density of discontinuous HAGBs. One may argue that CDRX still occurs at high strain levels, and that the saturation of the total discontinuous HAGB density could result from a dynamic equilibrium transformation of discontinuous HAGBs into continuous HAGBs. However, this is unlikely, as most discontinuous HAGBs have relatively low misorientation angles, typically between 15° and 35°, as shown in Fig. 5(c) and (d). If discontinuous HAGBs were indeed transforming into continuous HAGBs, the density of continuous HAGBs with misorientation angles from 15° to 35° would be particularly high. In fact, as seen in Fig. 3(c) and (d), the density of continuous HAGBs in the 15° to 35° range is comparatively lower than that of the other continuous HAGBs. Furthermore, as seen in Fig. 7(a) and (b), the density of both LAGBs and GNDs decreases when the alloy is deformed to higher strain levels, typically above $\varepsilon = 0.75$. Given that CDRX involves continuous transformation of LAGBs into HAGBs by increasing misorientation angles of LAGBs at the consumption of dislocations [15, 16], the decrease in both LAGB and GND densities hinders the

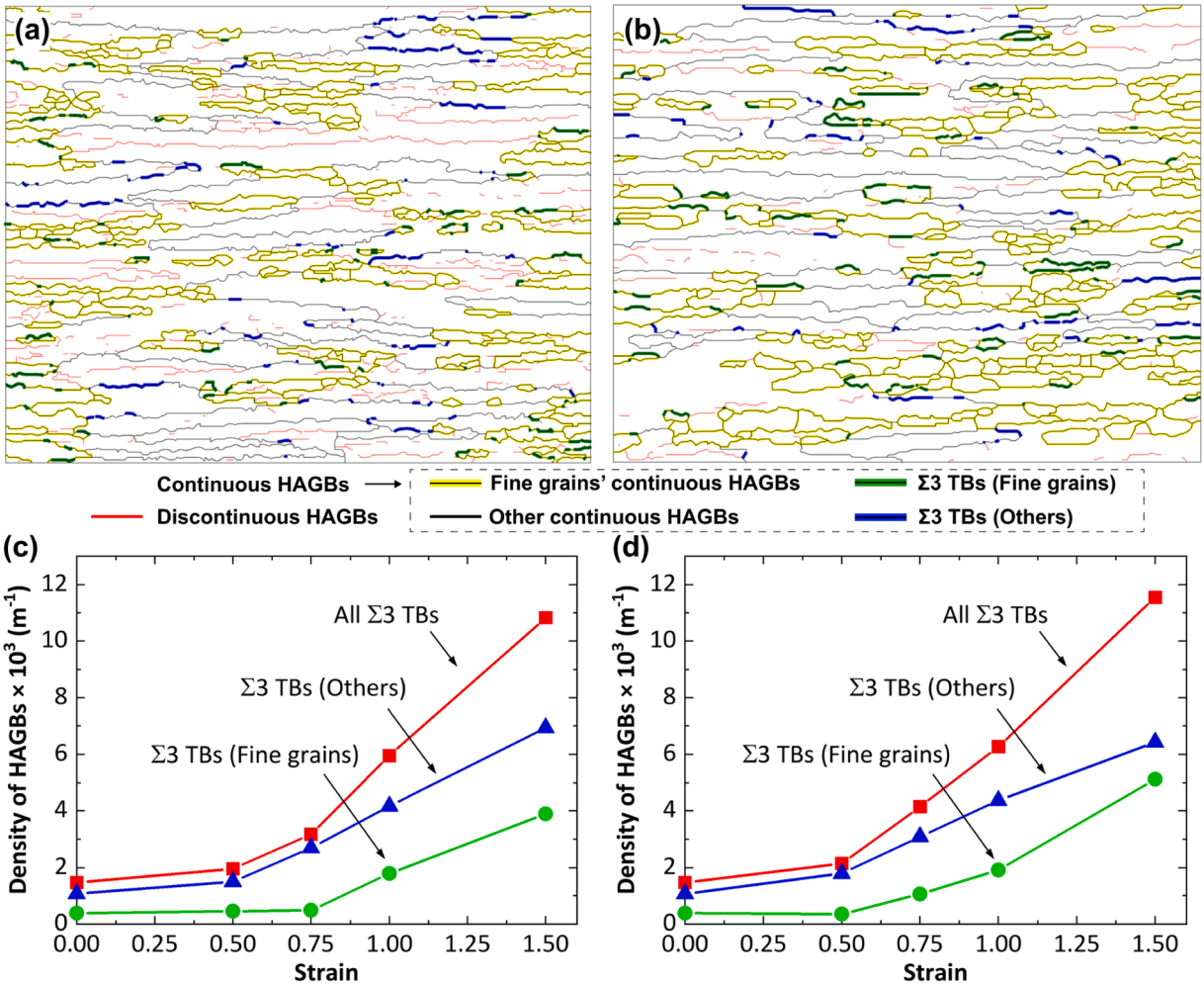

Fig. 11. Formation of Σ3 twin boundaries (TBs) exhibiting a misorientation angle of 60° ± 5° and a misorientation axis within 5° of ⟨111⟩ in AA6061 during hot compression tests, (a) and (b) Magnified regions showing Σ3 TBs deformed to 1.5 at different deformation conditions: (a) 400 °C and 0.1 s^{-1} (blue rectangle in Fig. 2 (a4)), (b) 475 °C and 0.1 s^{-1} (blue rectangle in Fig. 2(b4)), (c) and (d) Evolution of Σ3 TBs in continuous HAGBs of fine grains (perimeter ≤ 200 μm), and in the other continuous HAGBs excluding those of fine grains: (c) 400 °C and 0.1 s^{-1}, (d) 475 °C and 0.1 s^{-1} (For interpretation of the references to color in this figure legend, the reader is referred to the web version of this article.).

occurrence of CDRX.

The occurrence of GDRX presents a reverse trend as deformation progresses compared to the CDRX. As observed in Fig. 6, the density of HAGBs of fine equiaxed grains generated through GDRX remains unchanged in the initial stages of deformation. When the alloy is deformed to higher strain levels, specifically above $\varepsilon = 0.5$, the density of HAGBs of fine grains accelerates as deformation rises. This suggests that GDRX initiates at relatively high strain levels, slightly before the completion of CDRX. In addition, with further deformation to higher strain levels, such as $\varepsilon = 1.5$, the density of HAGBs of fine grains exceeds that of discontinuous HAGBs, particularly at higher temperatures. This suggests that GDRX surpasses CDRX and becomes the dominant DRX mechanism at higher strain levels. The occurrence of GDRX needs to meet several conditions, including the serrations of HAGBs and the flattening of original grains, which should typically have a thickness along the compression direction approximately 2 or 3 times the size of subgrains [26]. This explains why GDRX does not initiate in the early stages of deformation. For example, the original grains are not sufficiently flattened to meet the initiation criteria. One may speculate that the accumulation of discontinuous HAGBs through CDRX contributed to the acceleration of GDRX because the discontinuous HAGBs also become serrated, as seen in Fig. 8(e) and (f), and their presence facilitates the contact of HAGBs. However, this is unlikely, as the increase in fine grains' HAGBs at misorientation angles between 15° and 35° is significantly lower than for those at misorientation angles above 35°, as illustrated in Fig. 4(c) and (d).

Overall, CDRX occurs in the early stages of hot deformation, while GDRX initiates slightly before CDRX reaches saturation and accelerates at large strains. The acceleration of GDRX at large strains occurs because more grains become significantly flattened and reach the critical condition for GDRX [26,44]. This mechanism also applies to torsion and accumulative roll-bonding, where large deformations are typically achieved. Regarding CDRX, it results in the formation of discontinuous HAGBs. Additionally, as shown in Fig. 5(c) and (d), after reaching saturation at large strains, the misorientation angle distributions for discontinuous HAGBs remain unchanged as the deformation progresses further. This indicates that the discontinuous HAGBs remain stable as deformation continues. Therefore, the method used to distinguish between GDRX and CDRX based on the continuous and discontinuous characteristics of HAGBs can also be extended to other tests involving large strains, such as torsion.

4.3. Formation of ⟨110⟩ fibre texture and its impact on DRX

As observed in Fig. 9, the ⟨110⟩ fibre texture along the compression direction develops during hot deformation of AA6061. Specifically, the

⟨110⟩ texture forms in the early stages of deformation and tends to reach saturation at relatively high strain levels, specifically above $\varepsilon = 0.75$. It is interesting to notice that this evolution of the ⟨110⟩ texture is extremely similar to the evolution of CDRX in producing discontinuous HAGBs, as shown in Fig. 5(a) and (b). Therefore, there probably exists an essential connection between the formation of the ⟨110⟩ fiber texture and the occurrence of CDRX [20,70]. The formation of the ⟨110⟩ fiber texture along the compression direction is attributed to the FCC crystal lattice structure of AA6061 and crystal directions ⟨110⟩ are the most active slip directions. Similar phenomena have been reported in Refs. [16,30,71]. Additionally, a previous study [16] reports that, during hot compression of an aluminium AA1xxx with single crystals, CDRX initiates at a strain of 0.3 in ⟨111⟩ crystal, while at a strain of 0.9 in ⟨001⟩ crystal. In contrast, CDRX does not occur in ⟨110⟩ crystal. These findings suggest that the occurrence of CDRX can be influenced by the initial crystallographic orientation of the alloy. However, future effects are needed to directly disclose the mechanistic relationship between the texture formation and the occurrence of CDRX.

4.4. Kinetics of DRV and formation of Σ3 TBs

As observed in Fig. 7(a) and (b), the density of LAGBs accelerates at the onset of hot deformation along with the acceleration of the density of GNDs. The formation of LAGBs results from the occurrence of DRV at the rearrangement and consumption of GNDs [21], indicating that DRV initiates at the onset of hot deformation. Additionally, as deformation progresses, the kinetics of DRV increase, as evidenced by the continuous reduction in the density of GNDs at relatively high strain levels, specifically above $\varepsilon = 0.75$.

As seen in Fig. 3(c) and (d), the density of continuous HAGBs at relatively high misorientation angles between 52° and 61° particularly increases as hot deformation progresses. These continuous HAGBs include a large portion of Σ3 TBs (60° ⟨111⟩), as shown in Fig. 11(a) and (b), which are known for their low energy due to their highly ordered atomic structure [72,73]. As observed in Fig. 11(c) and (d), the formation of Σ3 TBs begins at the onset of hot deformation, but accelerates at relatively high strain levels, specifically above $\varepsilon = 0.75$. Additionally, the formation of Σ3 TBs in continuous HAGBs of fine grains is slightly delay compared to in the other continuous HAGBs excluding those of the fine grains. This is attributed to the formation of fine grains occurring at relatively high strain levels, as illustrated in Fig. 6(a) and (b). It is important to note that, as illustrated in Fig. 11, the Σ3 TBs are not associated with physical deformation twins or annealing twins, similarly to the phenomena reported in Refs. [61,63,64]. In fact, it is commonly recognised that neither type of twin typically forms in high SFE materials [74]. The formation kinetics of Σ3 TBs closely align with those of DRV, as the increase in Σ3 TBs correlates with a reduction in the density of GNDs and LAGBs at similarly high strain levels. In addition, higher temperatures result in a higher density of Σ3 TBs, as shown in Fig. 11(c) and (d). These observations indicate that the formation of Σ3 TBs is likely linked to the DRV process. In Ref. [21], DRV was identified as the sole restoration mechanism in aluminum alloys. Nevertheless, further investigation is required to fully elucidate their formation mechanisms. Additionally, as shown in Figs. 9 and 11, compared to the ⟨110⟩ fibre texture, which develops rapidly in the early stages of deformation and tends to saturate at large strains, Σ3 TBs form slowly at first and then accelerate at large strains. Considering that both fibre texture and TBs contribute to lower-energy configurations, it may suggest that ⟨110⟩ fibre texture develops first, potentially promoting TB formation. However, as strain increases, TB formation accelerates just as the fibre texture reaches saturation, indicating that TB formation does not directly correlate with fibre texture development.

It is worth noting that Σ3 TBs are not observed in discontinuous HAGBs even at high strain levels, as shown in Fig. 11(a) and (b) and Appendix E. In fact, as deformation progresses, the misorientation angles of discontinuous HAGBs show no obvious increase, with the density of HAGBs between 52° and 61° nearly zero, as shown in Fig. 5(c) and (d). Therefore, the discontinuous HAGBs differ significantly from the continuous HAGBs in their response to evolve into Σ3 TBs. One interesting finding is that Σ3 TBs are discontinuous segments, which closely resemble the discontinuous HAGBs produced through CDRX.

5. Conclusions

In this study, the kinetics of continuous dynamic recrystallisation (CDRX) and geometric dynamic recrystallisation (GDRX) in an aluminium alloy (AA6061) during hot compression tests have been investigated. The alloy was deformed at varying strain levels up to 1.5, and the resulting crystallographic microstructure was characterised within a large region using high-resolution electron backscatter diffraction (HR-EBSD) technology. By quantitively analysing the characteristics of high-angle grain boundaries (HAGBs), low-angle grain boundaries (LAGBs) and geometrically necessary dislocations (GNDs), the following conclusions can be drawn:

1) CDRX occurs during the initial stages of deformation, increases as deformation progresses, and eventually saturates to a certain value at relatively high strain levels. This saturated value is inversely proportional to deformation temperature, while directly proportional to strain rate. The decrease in the kinetics of CDRX with increasing deformation is attributed to the reduction in GNDs and LAGBs, which results from the occurrence of dynamic recovery (DRV).
2) GDRX leads to the generation of fine equiaxed grains with perimeters below 200 μm, particularly in the 25 to 75 μm range. Furthermore, GDRX initiates slightly before CDRX reaches saturation, and GDRX increases quickly as deformation rises. The density of HAGBs generated through GDRX can surpass that through CDRX, becoming the dominant DRX mechanism at high strain levels.
3) As deformation progresses, HAGBs with misorientation angles ranging from 52° to 61° are increasingly produced in continuous HAGBs, while they are not produced in discontinuous HAGBs. These HAGBs include Σ3 (60° ⟨111⟩) twin boundaries (TBs), which are firstly produced in original HAGBs and subsequently generated in new HAGBs of fine grains produced through GDRX

CRediT authorship contribution statement

Ruiqiang Zhang: Writing – original draft, Software, Methodology, Investigation, Formal analysis, Writing – review & editing. **Jieming S. Zhang:** Writing – review & editing, Validation. **Wei Wang:** Writing – review & editing, Investigation. **Yuanbo T. Tang:** Writing – review & editing, Validation. **Jun Jiang:** Writing – review & editing, Supervision, Methodology, Funding acquisition. **Roger C. Reed:** Writing – review & editing, Visualization. **Jianguo Lin:** Writing – review & editing, Methodology.

Declaration of interest

The authors declare that they have no known competing financial interests or personal relationships that could have appeared to influence the work reported in this paper.

Acknowledgements

This work was supported by the Engineering and Physical Sciences Research Council (EPSRC) [grant number EP/R001715/1] on “Lightform: Embedding Materials Engineering in Manufacturing with Light Alloys”.

Appendix A. Fine grains

Fig. A.1(a1)–(a4) and (b1)–(b4) presents the distribution maps of fine equiaxed grains with perimeters less than or equal to 200 μm in AA6061 samples deformed at different strain levels under conditions of 400 °C & 0.1 s^{-1} and 475 °C & 0.1 s^{-1}, respectively. Grains located at the map boundaries were excluded during the selection process. The fine grains are uniformly distributed across the alloy. In addition, the number of the fine grains increases sharply when the alloy is deformed to high strain levels, such as $\varepsilon = 1.5$.

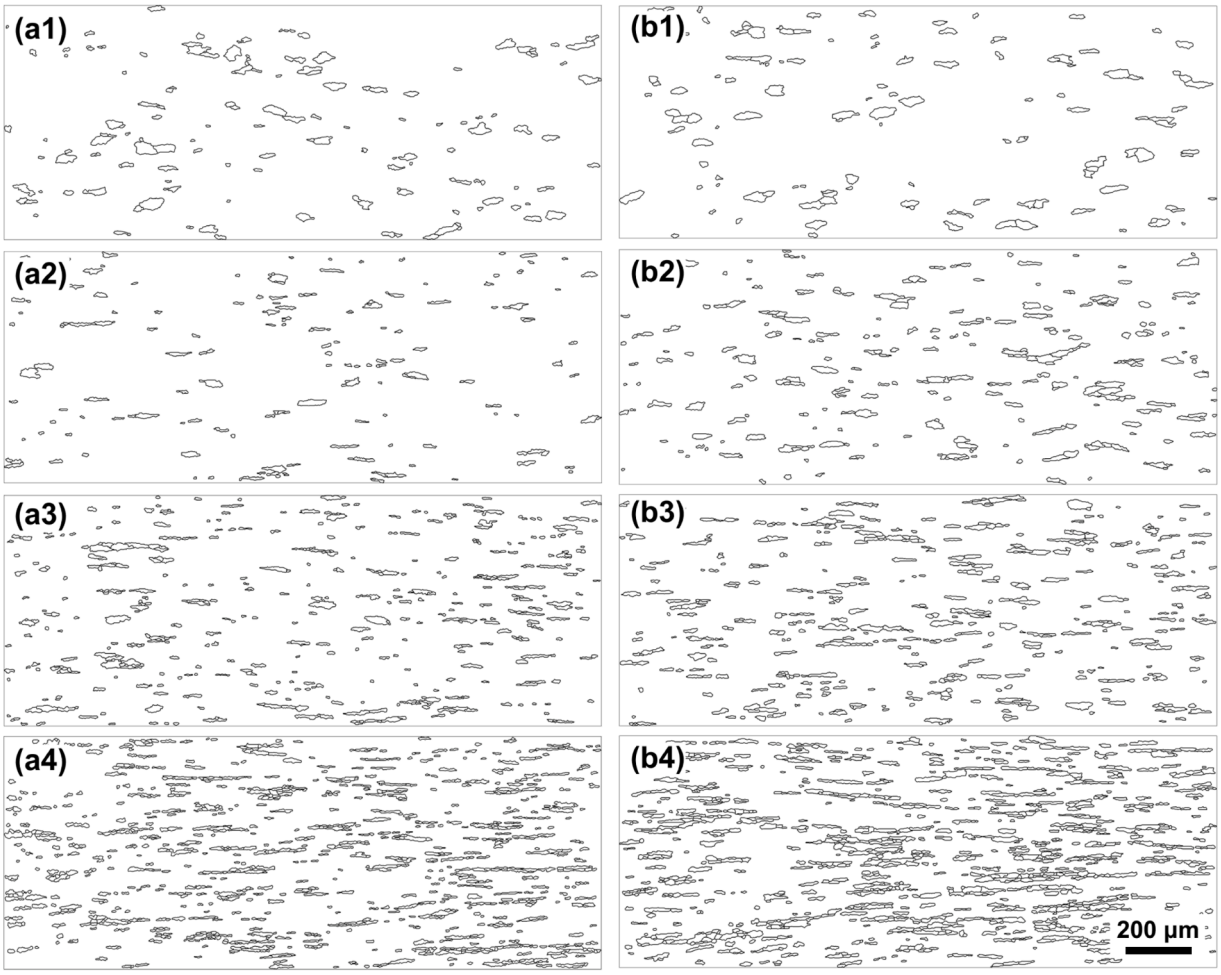

Fig. A.1. Selected HAGBs of fine grains with perimeters less than or equal to 200 μm in AA6061 deformed during hot compression tests at different strain levels: (a1)–(b1) 0.5, (a2)–(b2) 0.75, (a3)–(b3) 1 and (a4)–(b4) 1.5. Additionally, (a1)–(a4) at 400 °C and 0.1 s^{-1} and (b1)–(b4) 475 °C and 0.1 s^{-1}.

Appendix B. LAGBs and GND densities

Fig. B.1(a1)–(a4) and (b1)–(b4) displays distribution maps of LAGBs (blue lines), along with continuous HAGBs (black lines) and discontinuous HAGBs (red lines) in AA6061 samples deformed at different strain levels under conditions of 400 °C & 0.1 s^{-1} and 475 °C & 0.1 s^{-1}, respectively. As can be seen, LAGBs are nearly uniformly distributed across the maps at varying stain levels under both testing conditions. This indicates the rapid DRV occurring in this high SFE alloy during hot deformation, resulting in the formation of fine, equiaxed, steady subgrains. Additionally, higher temperatures reduce the density of LAGBs due to the enhanced DRV at elevated temperatures.

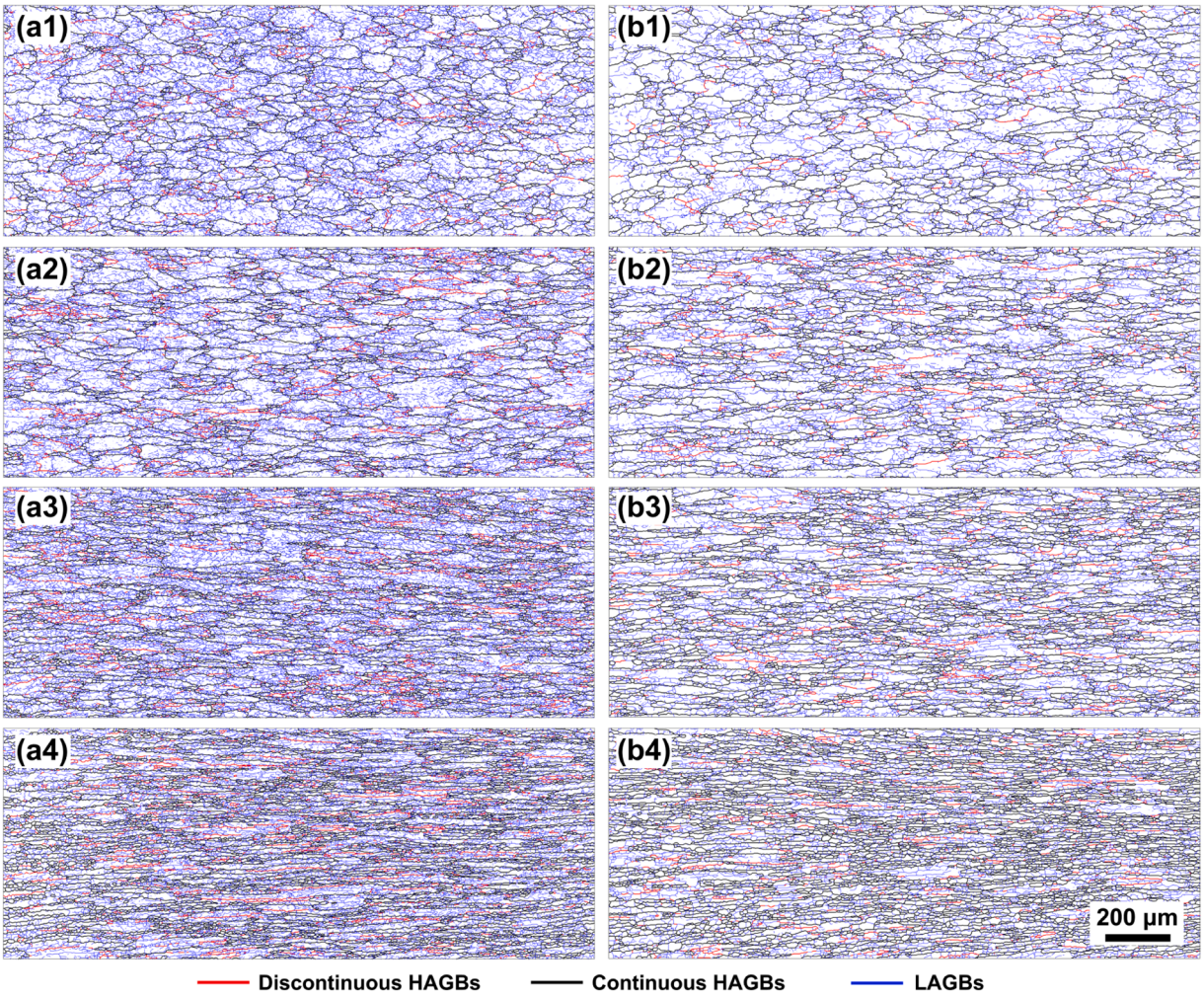

Fig. B.1. Maps showing distributions of LAGBs in AA6061 deformed during hot compression tests at different strain levels: (a1)–(b1) 0.5, (a2)–(b2) 0.75, (a3)–(b3) 1 and (a4)–(b4) 1.5. Additionally, (a1)–(a4) at 400 °C and 0.1 s^{-1} and (b1)–(b4) 475 °C and 0.1 s^{-1}.

Fig. B.2(a1)–(a4) and (b1)–(b4) shows distribution maps of GND densities in AA6061 samples deformed at different strain levels under conditions of 400 °C & 0.1 s^{-1} and 475 °C & 0.1 s^{-1}, respectively. Similarly to the LAGBs, the distribution of GND densities, with varying values, is relatively uniform across the characterised EBSD map. Furthermore, the GND density decreases with increasing deformation temperature due to the enhanced DRV.

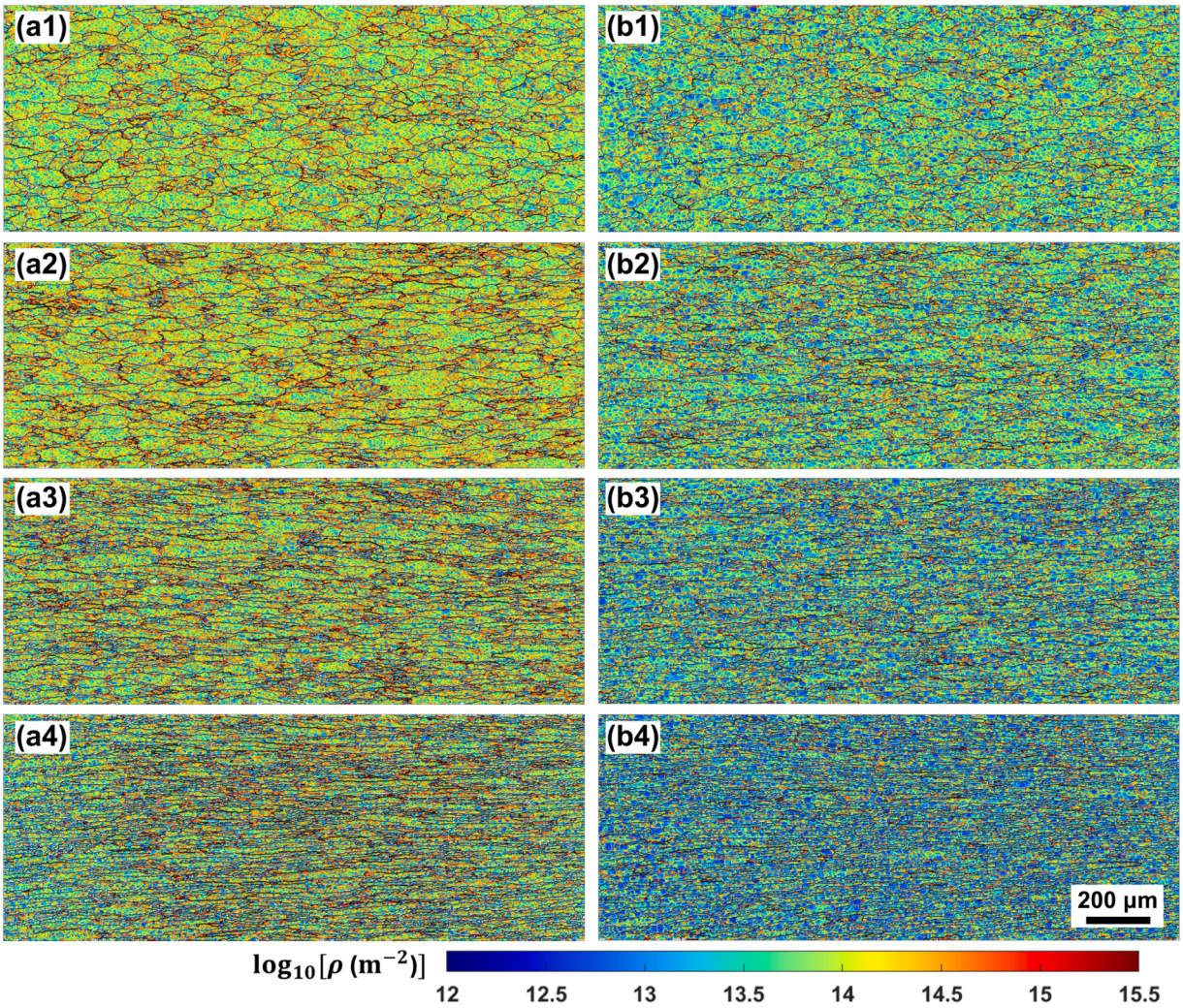

Fig. B.2. Maps showing GND densities in AA6061 deformed during hot compression tests at different strain levels: (a1)–(b1) 0.5, (a2)–(b2) 0.75, (a3)–(b3) 1 and (a4)–(b4) 1.5. Additionally, (a1)–(a4) at 400 °C and 0.1 s^{-1} and (b1)–(b4) 475 °C and 0.1 s^{-1}.

Appendix C. Curvature of HAGBs

Fig. C.1(a1)–(a4) and (b1)–(b4) displays distribution maps of the local curvature values for all HAGBs comprising of both continuous HAGBs and discontinuous HAGBs, for AA6061 samples deformed at different strain levels under conditions of 400 °C & 0.1 s^{-1} and 475 °C & 0.1 s^{-1}, respectively. The calculation method of the local curvature values is detailed in Section 3.3. The HAGBs with relatively high curvature values are uniformly distributed across the maps. Furthermore, as deformation progresses, a significant fraction of HAGBs with low curvature values remains distributed uniformly throughout the alloy. This indicates that, during hot deformation, only a limited fraction of HAGBs become serrated.

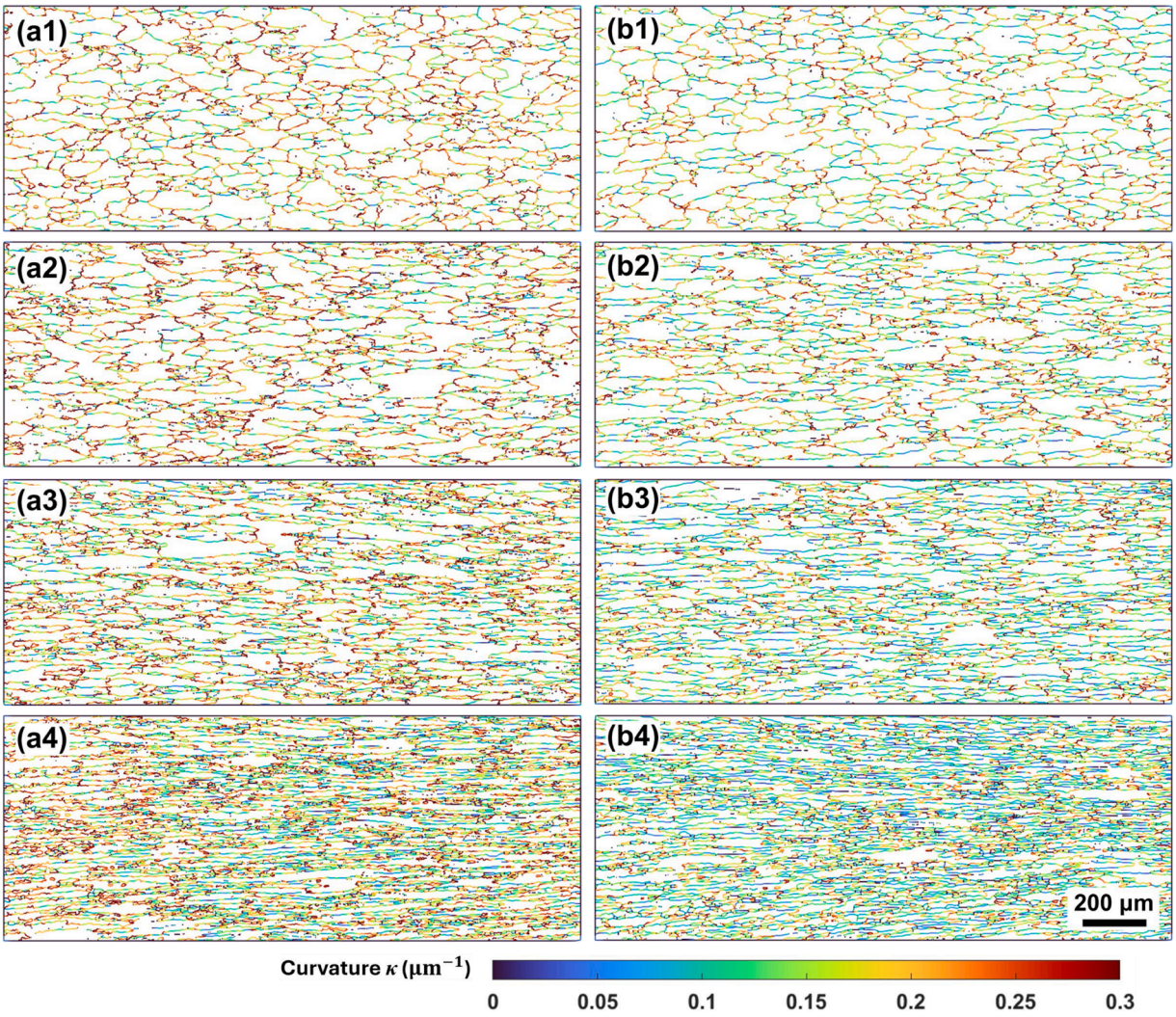

Fig. C.1. Curvature of all HAGBs comprising the continuous and discontinuous HAGBs in AA6061 deformed during hot compression tests to different strain levels: (a1)–(b1) 0.5, (a2)–(b2) 0.75, (a3)–(b3) 1 and (a4)–(b4) 1.5. Additionally, (a1)–(a4) at 400 °C and 0.1 s^{-1} and (b1)–(b4) 475 °C and 0.1 s^{-1}.

Appendix D. IPF maps along compressive direction

Fig. D.1(a1)–(a4) and (b1)–(b4) displays the IPF maps along the Y-axis (compression direction) for AA6061 samples deformed at different strain levels under conditions of 400 °C & 0.1 s^{-1} and 475 °C & 0.1 s^{-1}, respectively. Most grains present a green colour, indicating that the ⟨110⟩ crystal directions of these grains align with the compression direction, namely the formation of a ⟨110⟩ fibre texture. As deformation progresses, the fraction of area of the grains in the green colour increases, indicating that the fibre texture becomes stronger.

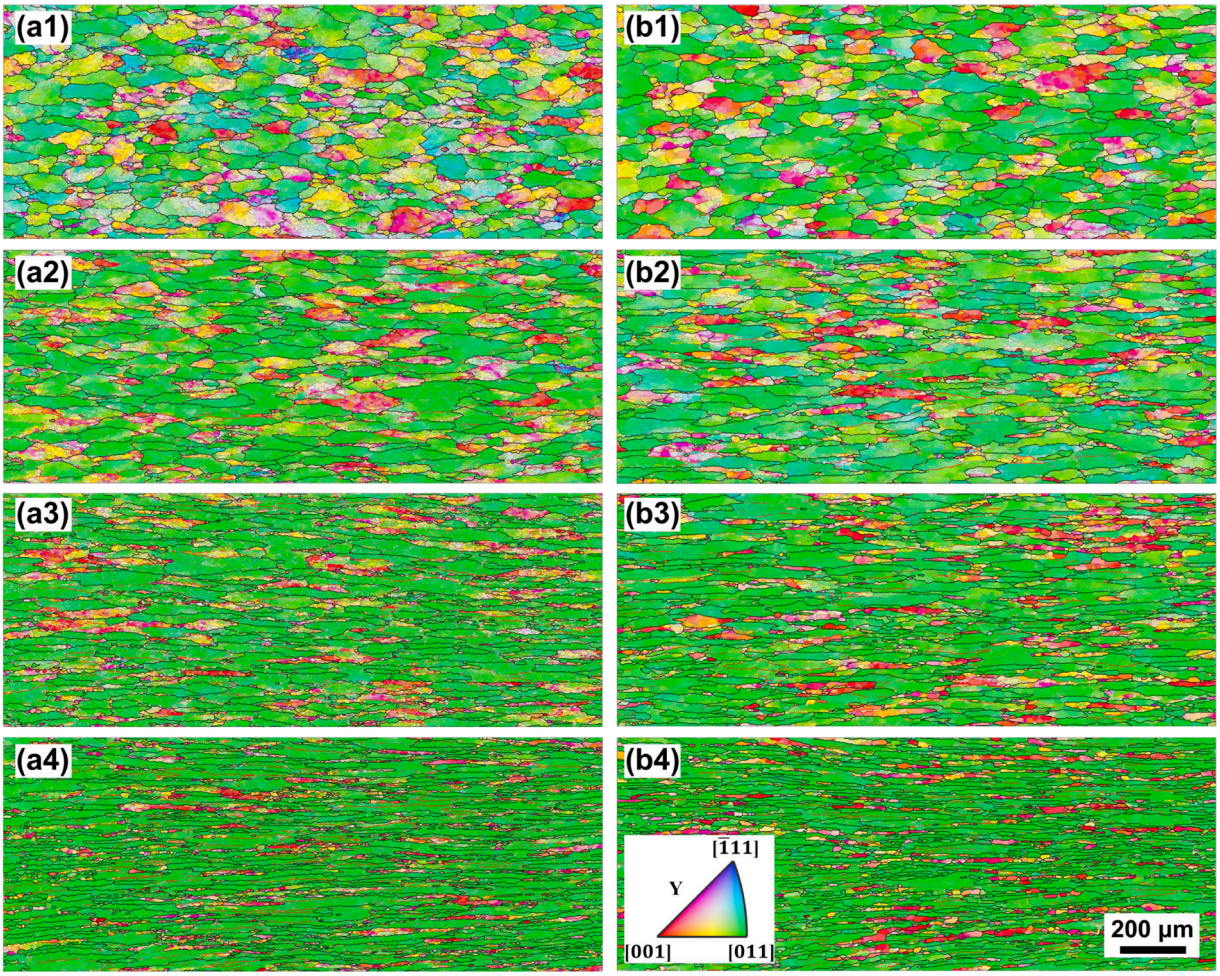

Fig. D.1. IPF maps along the Y-axis (compression direction) for AA6061 deformed during hot compression tests at different strain levels: (a1)–(b1) 0.5, (a2)–(b2) 0.75, (a3)–(b3) 1 and (a4)–(b4) 1.5. Additionally, (a1)–(a4) at 400 °C and 0.1 s^{-1} and (b1)–(b4) 475 °C and 0.1 s^{-1}.

Appendix E. HAGBs at high misorientation angles and Σ3 TBs

Fig. E.1(a1)–(a4) and (b1)–(b4) shows distribution maps of continuous HAGBs at relatively high misorientation angles θ ranging from 52° to 61° (blue lines), together with the other continuous HAGBs (black lines) and discontinuous HAGBs (red lines), in AA6061 samples deformed at different strain levels under conditions of 400 °C & 0.1 s^{-1} and 475 °C & 0.1 s^{-1}, respectively. It should be noted that the density of the discontinuous HAGBs with $52° \leq \theta \leq 61°$ is nearly zero. As seen, the continuous HAGBs with $52° \leq \theta \leq 61°$ are uniformly distributed across the maps. Furthermore, as deformation progresses, their density increases significantly.

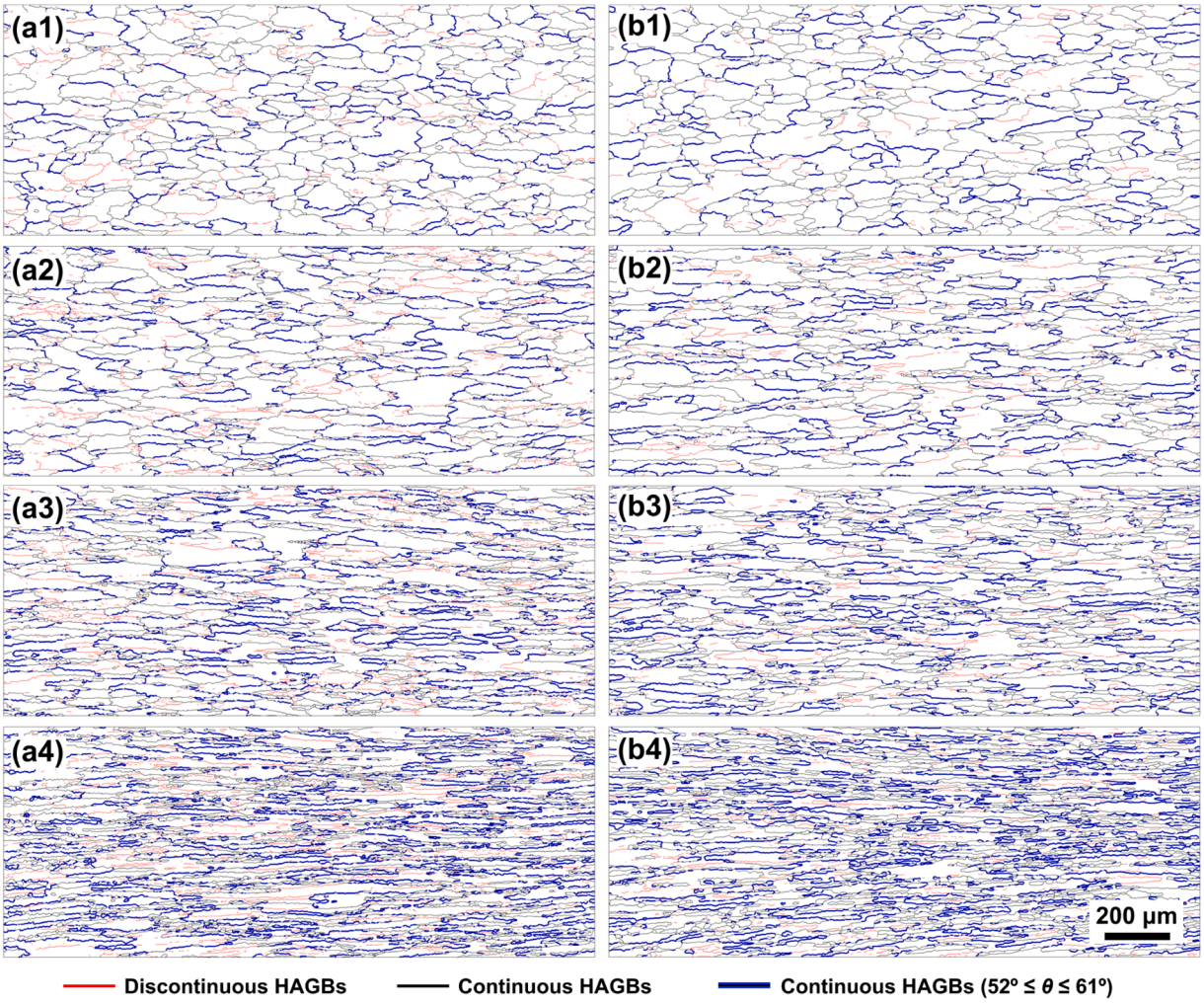

Fig. E.1. Continuous HAGBs with misorientation angles ranging from 52° to 61° in AA6061 deformed during hot compression tests at different strain levels: (a1)–(b1) 0.5, (a2)–(b2) 0.75, (a3)–(b3) 1 and (a4)–(b4) 1.5. Additionally, (a1)–(a4) at 400 °C and 0.1 s^{-1} and (b1)–(b4) 475 °C and 0.1 s^{-1}.

Fig. E.2(a1)–(a4) and (b1)–(b4) shows distribution maps of Σ3 TBs (60° ⟨111⟩) in AA6061 samples deformed at different strain levels under conditions of 400 °C & 0.1 s^{-1} and 475 °C & 0.1 s^{-1}, respectively. To differentiate Σ3 TBs in the continuous HAGBs of fine grains (perimeter ≤ 200 μm) from those in the other continuous HAGBs, they are coloured blue and green, respectively. In addition, fine grains are shown in yellow. As seen, Σ3 TBs in both continuous HAGBs of fine grains and other continuous HAGBs are uniformly distributed across the maps. Furthermore, when the alloy was deformed to high strain levels, such as $\varepsilon = 1.5$, the density of these Σ3 TBs increases significantly.

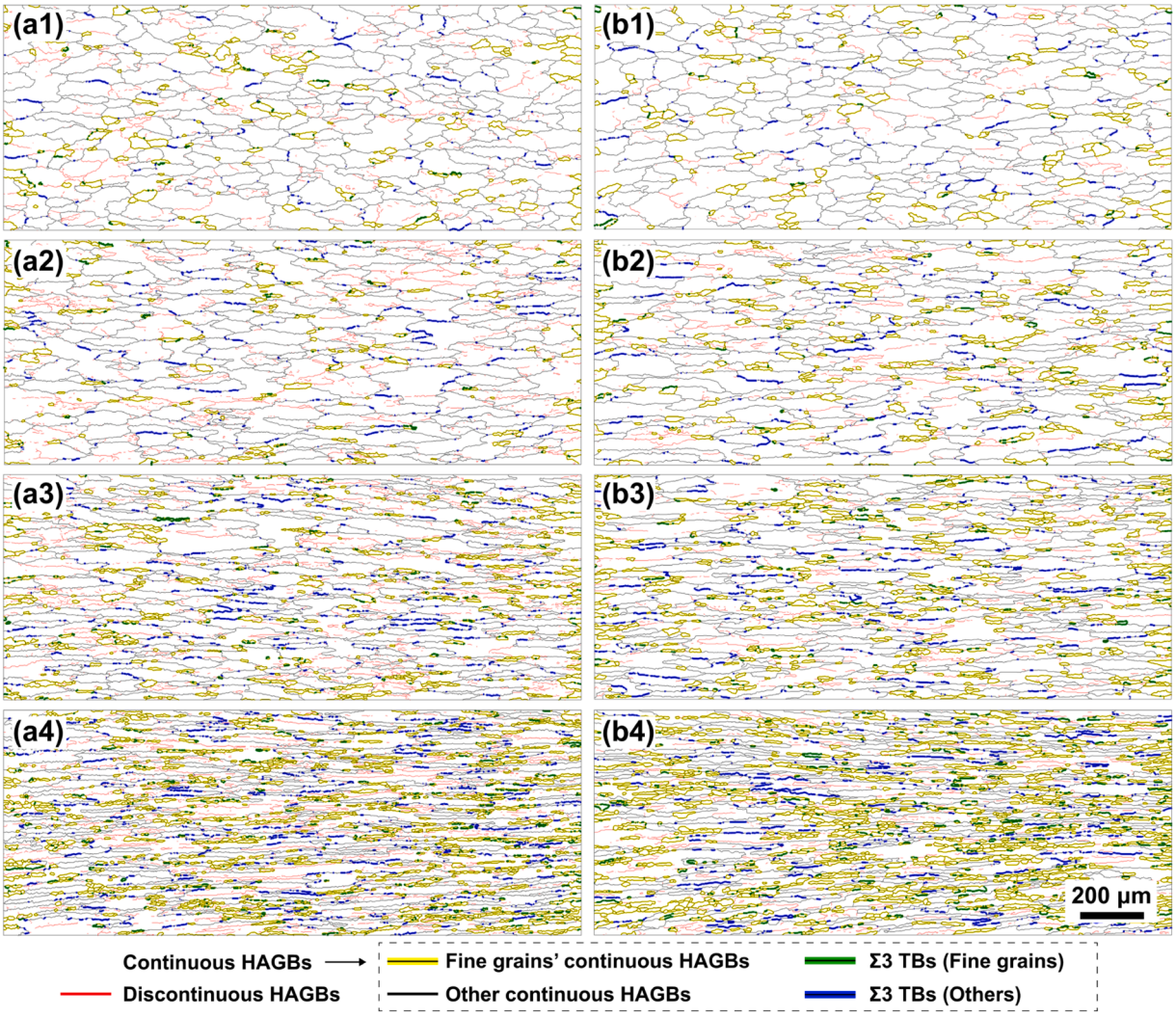

Fig. E.2. Σ3 twin boundaries (TBs) in the continuous HAGBs of fine grains (perimeter ≤ 200 μm) and in the other continuous HAGBs excluding those of the fine grains in AA6061 deformed during hot compression tests at different strain levels: (a1)–(b1) 0.5, (a2)–(b2) 0.75, (a3)–(b3) 1 and (a4)–(b4) 1.5. Additionally, (a1)–(a4) at 400 °C and 0.1 s^{-1} and (b1)–(b4) 475 °C and 0.1 s^{-1}.

References

[1] R. Zhang, W. Wang, J. Lin, T.A. Dean, An indirect hot form and quench (HFQ) for manufacturing components of aluminum alloy sheets and comparison with direct HFQ, Int. J. Mach. Tool. Manufact. 192 (2023), https://doi.org/10.1016/j.ijmachtools.2023.104073.

[2] M. Shih, J. Miao, M. Mills, M. Ghazisaeidi, Stacking fault energy in concentrated alloys, Nat. Commun. 12 (2021) 3590, https://doi.org/10.1038/s41467-021-23860-z.

[3] F.J. Humphreys, A unified theory of recovery, recrystallization and grain growth, based on the stability and growth of cellular microstructures—I. The basic model, Acta Mater. 45 (1997) 4231–4240, https://doi.org/10.1016/S1359-6454(97)00070-0.

[4] H.J. McQueen, E. Evangelista, Substructures in aluminium from dynamic and static recovery, Czechoslovak J. Phys. B 38 (1988) 359–372, https://doi.org/10.1007/BF01605405.

[5] C.S. Patil, S. Chakraborty, S.R. Niezgoda, Cross slip based dynamic recovery during plane strain compression of aluminium and its role in preferential nucleation of the cube-oriented recrystallized grains, Acta Mater. 272 (2024), https://doi.org/10.1016/j.actamat.2024.119913.

[6] T. Sakai, A. Belyakov, R. Kaibyshev, H. Miura, J.J. Jonas, Dynamic and post-dynamic recrystallization under hot, cold and severe plastic deformation conditions, Prog. Mater. Sci. 60 (2014) 130–207, https://doi.org/10.1016/j.pmatsci.2013.09.002.

[7] H. Asgharzadeh, H.J. McQueen, Grain growth and stabilisation of nanostructured aluminium at high temperatures: review, Mater. Sci. Technol. 31 (2015) 1016–1034, https://doi.org/10.1179/1743284714y.0000000706.

[8] K. Huang, R.E. Logé, A review of dynamic recrystallization phenomena in metallic materials, Mater. Des. 111 (2016) 548–574, https://doi.org/10.1016/j.matdes.2016.09.012.

[9] R.D. Doherty, D.A. Hughes, F.J. Humphreys, J.J. Jonas, D.J. Jensen, M.E. Kassner, W.E. King, T.R. McNelley, H.J. McQueen, A.D. Rollett, Current issues in recrystallization: a review, Mater. Sci. Eng.: A 238 (1997) 219–274, https://doi.org/10.1016/S0921-5093(97)00424-3.

[10] P. Yu, C. Wu, L. Shi, Analysis and characterization of dynamic recrystallization and grain structure evolution in friction stir welding of aluminum plates, Acta Mater. 207 (2021), https://doi.org/10.1016/j.actamat.2021.116692.

[11] J. Zhang, Y. Yi, S. Huang, X. Mao, H. He, J. Tang, W. Guo, F. Dong, Dynamic recrystallization mechanisms of 2195 aluminum alloy during medium/high temperature compression deformation, Mater. Sci. Eng.: A 804 (2021), https://doi.org/10.1016/j.msea.2020.140650.

[12] Y. Wang, G. Zhao, L. Sun, X. Wang, Effects of strain and strain rate on dynamic recrystallization and solid-state welding behaviors of aluminum alloys, J. Mater. Res. Technol. 29 (2024) 4036–4051, https://doi.org/10.1016/j.jmrt.2024.02.138.

[13] S. Jiang, J. Lv, Z. Shi, J. Lin, A study of dynamic recovery and recrystallisation mechanisms in aluminium alloy AA7050 at different thermomechanical processing conditions, Mater. Sci. Eng.: A 914 (2024), https://doi.org/10.1016/j.msea.2024.147117.

[14] H. Li, Y. Huang, Y. Liu, Dynamic recrystallization mechanisms of as-forged Al–Zn–Mg-(Cu) aluminum alloy during hot compression deformation, Mater. Sci. Eng.: A 878 (2023), https://doi.org/10.1016/j.msea.2023.145236.

[15] S. Gourdet, F. Montheillet, A model of continuous dynamic recrystallization, Acta Mater. 51 (2003) 2685–2699, https://doi.org/10.1016/s1359-6454(03)00078-8.

[16] S. Gourdet, F. Montheillet, An experimental study of the recrystallization mechanism during hot deformation of aluminium, Mater. Sci. Eng.: A 283 (2000) 274–288, https://doi.org/10.1016/S0921-5093(00)00733-4.

[17] K. Wang, C. Zhang, Z. Cheng, H. Zhao, Z. Meng, L. Chen, G. Zhao, Dynamic evolution of the T1 phase and its effect on continuous dynamic recrystallization in Al–Cu–Li alloys, Int. J. Plast. 175 (2024), https://doi.org/10.1016/j.ijplas.2024.103948.
[18] X. Feng, Y. Wang, Q. Huang, H. Liu, Z. Zhang, The dynamic recrystallization microstructure characteristics and the effects on static recrystallization and mechanical properties of Al–Mg–Si alloy, Mater. Sci. Eng.: A 899 (2024), https://doi.org/10.1016/j.msea.2024.146454.
[19] C. Zhang, C. Wang, R. Guo, G. Zhao, L. Chen, W. Sun, X. Wang, Investigation of dynamic recrystallization and modeling of microstructure evolution of an Al-Mg-Si aluminum alloy during high-temperature deformation, J. Alloy. Compd. 773 (2019) 59–70, https://doi.org/10.1016/j.jallcom.2018.09.263.
[20] S.F. Chen, D.Y. Li, S.H. Zhang, H.N. Han, H.W. Lee, M.G. Lee, Modelling continuous dynamic recrystallization of aluminum alloys based on the polycrystal plasticity approach, Int. J. Plast. 131 (2020), https://doi.org/10.1016/j.ijplas.2020.102710.
[21] H.J. McQueen, W. Blum, Dynamic recovery: sufficient mechanism in the hot deformation of Al (B99.99), Mater. Sci. Eng. A 290 (2000) 95–107, https://doi.org/10.1016/S0921-5093(00)00933-3.
[22] H.J. McQueen, M.E. Kassner, Comments on 'a model of continuous dynamic recrystallization' proposed for aluminum, Scr. Mater. 51 (2004) 461–465, https://doi.org/10.1016/j.scriptamat.2004.05.027.
[23] H.J. McQueen, O. Knustad, N. Ryum, J.K. Solberg, Microstructural evolution in Al deformed to strains of 60 at 400 °C, Scripta Metallurg. 19 (1985) 73–78, https://doi.org/10.1016/0036-9748(85)90268-6.
[24] J.K. Solberg, H.J. McQueen, N. Ryum, E. Nes, Influence of ultra-high strains at elevated temperatures on the microstructure of aluminium. Part I, Philosoph. Magaz. A 60 (1989) 447–471, https://doi.org/10.1080/01418618908213872.
[25] H.J. McQueen, J.K. Solberg, N. Ryum, E. Nes, Evolution of flow stress in aluminium during ultra-high straining at elevated temperatures. Part II, Philosoph. Magaz. A 60 (1989) 473–485, https://doi.org/10.1080/01418618908213873.
[26] W. Blum, Q. Zhu, R. Merkel, H.J. McQueen, Geometric dynamic recrystallization in hot torsion of A1-5Mg-0.6Mn (AA5083), Mater. Sci. Eng. A 205 (1996) 23–30, https://doi.org/10.1016/0921-5093(95)09990-5.
[27] D. Li, H. Liu, S. Du, X. Li, Y. Gao, Y. Zuo, Investigation on material flow and microstructural evolution mechanism in non-thinning and penetrating friction stir welded Al–Cu aluminum alloy, Mater. Sci. Eng.: A 864 (2023), https://doi.org/10.1016/j.msea.2022.144572.
[28] L.D. Pari, W.Z. Misiolek, Theoretical predictions and experimental verification of surface grain structure evolution for AA6061 during hot rolling, Acta Mater. 56 (2008) 6174–6185, https://doi.org/10.1016/j.actamat.2008.08.050.
[29] X. Zhang, Z. Luo, G. Xie, H. Yu, Z. Liu, J. Yang, Interface microstructure and bonding mechanisms of 7050 aluminum alloy thick plates produced by vacuum roll cladding, Mater. Sci. Eng.: A 850 (2022), https://doi.org/10.1016/j.msea.2022.143582.
[30] R. Zhang, J.-H. Zheng, J. Jiang, Dynamic recrystallisation: a quantitative study on grain boundary characteristics and dependence on temperature and strain rate in an aluminium alloy, Acta Mater. 278 (2024), https://doi.org/10.1016/j.actamat.2024.120266.
[31] S. Wang, J.R. Luo, L.G. Hou, J.S. Zhang, L.Z. Zhuang, Physically based constitutive analysis and microstructural evolution of AA7050 aluminum alloy during hot compression, Mater. Des. 107 (2016) 277–289, https://doi.org/10.1016/j.matdes.2016.06.023.
[32] A. Gholinia, F.J. Humphreys, P.B. Prangnell, Production of ultra-fine grain microstructures in Al–Mg alloys by coventional rolling, Acta Mater. 50 (2002) 4461–4476, https://doi.org/10.1016/S1359-6454(02)00253-7.
[33] K.T. Son, C.H. Cho, M.G. Kim, J.W. Lee, Two-stage dynamic recrystallization and texture evolution in Al-7Mg alloy during hot torsion, Int. J. Miner. Metall. Mater. 31 (2024) 1900–1911, https://doi.org/10.1007/s12613-024-2877-9.
[34] T. Sakai, H. Miura, A. Goloborodko, O. Sitdikov, Continuous dynamic recrystallization during the transient severe deformation of aluminum alloy 7475, Acta Mater. 57 (2009) 153–162, https://doi.org/10.1016/j.actamat.2008.09.001.
[35] O. Sitdikov, T. Sakai, E. Avtokratova, R. Kaibyshev, K. Tsuzaki, Y. Watanabe, Microstructure behavior of Al–Mg–Sc alloy processed by ECAP at elevated temperature, Acta Mater. 56 (2008) 821–834, https://doi.org/10.1016/j.actamat.2007.10.029.
[36] I. Mazurina, T. Sakai, H. Miura, O. Sitdikov, R. Kaibyshev, Grain refinement in aluminum alloy 2219 during ECAP at 250 °C, Mater. Sci. Eng.: A 473 (2008) 297–305, https://doi.org/10.1016/j.msea.2007.04.112.
[37] Y. Li, B. Gu, S. Jiang, Y. Liu, Z. Shi, J. Lin, A CDRX-based material model for hot deformation of aluminium alloys, Int. J. Plast. 134 (2020), https://doi.org/10.1016/j.ijplas.2020.102844.
[38] S. Zhu, E. Borodin, A.P. Jivkov, Discrete modelling of continuous dynamic recrystallisation by modified Metropolis algorithm, Computat. Mater. Sci. 234 (2024), https://doi.org/10.1016/j.commatsci.2024.112804.
[39] L.S. Tóth, Y. Estrin, R. Lapovok, C. Gu, A model of grain fragmentation based on lattice curvature, Acta Mater. 58 (2010) 1782–1794, https://doi.org/10.1016/j.actamat.2009.11.020.
[40] L. Liu, Y. Wu, A.S. Ahmad, A novel simulation of continuous dynamic recrystallization process for 2219 aluminium alloy using cellular automata technique, Mater. Sci. Eng.: A 815 (2021), https://doi.org/10.1016/j.msea.2021.141256.
[41] H.K. Zhang, H. Xiao, X.W. Fang, Q. Zhang, R.E. Logé, K. Huang, A critical assessment of experimental investigation of dynamic recrystallization of metallic materials, Mater. Des. 193 (2020), https://doi.org/10.1016/j.matdes.2020.108873.
[42] M.E. Kassner, S.R. Barrabes, New developments in geometric dynamic recrystallization, Mater. Sci. Eng.: A 410-411 (2005) 152–155, https://doi.org/10.1016/j.msea.2005.08.052.
[43] Z.C. Sun, H.L. Wu, J. Cao, Z.K. Yin, Modeling of continuous dynamic recrystallization of Al-Zn-Cu-Mg alloy during hot deformation based on the internal-state-variable (ISV) method, Int. J. Plast. 106 (2018) 73–87, https://doi.org/10.1016/j.ijplas.2018.03.002.
[44] H.J. McQueen, Development of dynamic recrystallization theory, Mater. Sci. Eng.: A 387-389 (2004) 203–208, https://doi.org/10.1016/j.msea.2004.01.064.
[45] F.J. Humphreys, Characterisation of fine-scale microstructures by electron backscatter diffraction (EBSD), Scr. Mater. 51 (2004) 771–776, https://doi.org/10.1016/j.scriptamat.2004.05.016.
[46] A.J. Wilkinson, T.B. Britton, Strains, planes, and EBSD in materials science, Mater. Today 15 (2012) 366–376, https://doi.org/10.1016/s1369-7021(12)70163-3.
[47] S. Shekhar, N.K. Sharma, S. Sahu, S. Misra, Electron Backscatter Diffraction Technique: Fundamentals to Applications, Springer, Singapore, 2022.
[48] R. Hielscher, MTEX, 2024. https://mtex-toolbox.github.io/index. Accessed 01/01/2022.
[49] Dynamic Systems Inc, Gleeble® Thermal-Mechanical Simulators, 2024. https://gleeble.com/. Accessed 01/02/2024.
[50] S. Kobayashi, T. Maruyama, S. Tsurekawa, T. Watanabe, Grain boundary engineering based on fractal analysis for control of segregation-induced intergranular brittle fracture in polycrystalline nickel, Acta Mater. 60 (2012) 6200–6212, https://doi.org/10.1016/j.actamat.2012.07.065.
[51] Y.T. Zhu, J. Narayan, J.P. Hirth, S. Mahajan, X.L. Wu, X.Z. Liao, Formation of single and multiple deformation twins in nanocrystalline fcc metals, Acta Mater. 57 (2009) 3763–3770, https://doi.org/10.1016/j.actamat.2009.04.020.
[52] N. Bozzolo, M. Bernacki, Viewpoint on the formation and evolution of annealing twins during thermomechanical processing of FCC metals and alloys, Metallurg. Mater. Transact. A 51 (2020) 2665–2684, https://doi.org/10.1007/s11661-020-05772-7.
[53] Y. Nie, Y.T. Chang, M.A. Charpagne, Origins of twin boundaries in additive manufactured stainless steels, Acta Mater. 275 (2024), https://doi.org/10.1016/j.actamat.2024.120035.
[54] L. Li, Z. Zhang, P. Zhang, Z. Zhang, A review on the fatigue cracking of twin boundaries: crystallographic orientation and stacking fault energy, Prog. Mater. Sci. 131 (2023), https://doi.org/10.1016/j.pmatsci.2022.101011.
[55] X. Li, J. Zhang, Y. Cui, M.B. Djukic, H. Feng, Y. Wang, Review of the hydrogen embrittlement and interactions between hydrogen and microstructural interfaces in metallic alloys: grain boundary, twin boundary, and nano-precipitate, Int. J. Hydrog. Energy 72 (2024) 74–109, https://doi.org/10.1016/j.ijhydene.2024.05.257.
[56] V. Randle, Twinning-related grain boundary engineering, Acta Mater. 52 (2004) 4067–4081, https://doi.org/10.1016/j.actamat.2004.05.031.
[57] K. Lu, L. Lu, S. Suresh, Strengthening materials by engineering coherent internal boundaries at the nanoscale, Science 324 (2009) 349–352, https://doi.org/10.1126/science.1159610.
[58] C.M. Barr, A.C. Leff, R.W. Demott, R.D. Doherty, M.L. Taheri, Unraveling the origin of twin related domains and grain boundary evolution during grain boundary engineering, Acta Mater. 144 (2018) 281–291, https://doi.org/10.1016/j.actamat.2017.10.007.
[59] M. Chen, E. Ma, K.J. Hemker, H. Sheng, Y. Wang, X. Cheng, Deformation twinning in nanocrystalline aluminum, Science 300 (2003) 1275–1277, https://doi.org/10.1126/science.1083727.
[60] D.M. Saylor, B.S. El Dasher, A.D. Rollett, G.S. Rohrer, Distribution of grain boundaries in aluminum as a function of five macroscopic parameters, Acta Mater. 52 (2004) 3649–3655, https://doi.org/10.1016/j.actamat.2004.04.018.
[61] H. Jia, S. Jin, Y. Li, Formation of Σ3{110} incoherent twin boundaries through geometrically necessary boundaries in an Al-8Zn alloy subjected to one pass of equal channel angular pressing, J. Alloy. Compd. 762 (2018) 190–195, https://doi.org/10.1016/j.jallcom.2018.05.168.
[62] J.Y. Liu, J.Q. Xiang, C. Li, L. Lu, Z.Y. Zhong, S.N. Luo, Annealing twins in high purity aluminium processed by dynamic equal channel angular pressing, Mater. Sci. Technol. 36 (2020) 1215–1220, https://doi.org/10.1080/02670836.2020.1764275.
[63] S. Ahmad, T. Brink, C.H. Liebscher, G. Dehm, Microstates and defects of incoherent Σ3 [111]twin boundaries in aluminum, Acta Mater. 243 (2023), https://doi.org/10.1016/j.actamat.2022.118499.
[64] S. Saood, T. Brink, C.H. Liebscher, G. Dehm, Influence of variation in grain boundary parameters on the evolution of atomic structure and properties of [111] tilt boundaries in aluminum, Acta Mater. 268 (2024), https://doi.org/10.1016/j.actamat.2024.119732.
[65] K. Lu, Stabilizing nanostructures in metals using grain and twin boundary architectures, Nat. Rev. Mater. 1 (2016), https://doi.org/10.1038/natrevmats.2016.19.
[66] W. Pantleon, Resolving the geometrically necessary dislocation content by conventional electron backscattering diffraction, Scr. Mater. 58 (2008) 994–997, https://doi.org/10.1016/j.scriptamat.2008.01.050.
[67] Y.T. Tang, P. Karamched, J. Liu, J.C. Haley, R.C. Reed, A.J. Wilkinson, Grain boundary serration in nickel alloy inconel 600: quantification and mechanisms, Acta Mater. 181 (2019) 352–366, https://doi.org/10.1016/j.actamat.2019.09.037.
[68] D. Ponge, G. Gottstein, Necklace formation during dynamic recrystallization: mechanisms and impact on flow behavior, Acta Mater. 46 (1998) 69–80, https://doi.org/10.1016/S1359-6454(97)00233-4.

[69] A. Deshpande, A. Tofangchi, K. Hsu, Microstructure evolution of Al6061 and copper during ultrasonic energy assisted compression, Mater. Charact. 153 (2019) 240–250, https://doi.org/10.1016/j.matchar.2019.05.005.
[70] C.D. Barrett, A. Imandoust, A.L. Oppedal, K. Inal, M.A. Tschopp, H. El Kadiri, Effect of grain boundaries on texture formation during dynamic recrystallization of magnesium alloys, Acta Mater. 128 (2017) 270–283, https://doi.org/10.1016/j.actamat.2017.01.063.
[71] X.H. Fan, M. Li, D.Y. Li, Y.C. Shao, S.R. Zhang, Y.H. Peng, Dynamic recrystallisation and dynamic precipitation in AA6061 aluminium alloy during hot deformation, Mater. Sci. Technol. 30 (2014) 1263–1272, https://doi.org/10.1179/1743284714y.0000000538.
[72] J. Wang, N. Li, O. Anderoglu, X. Zhang, A. Misra, J.Y. Huang, J.P. Hirth, Detwinning mechanisms for growth twins in face-centered cubic metals, Acta Mater. 58 (2010) 2262–2270, https://doi.org/10.1016/j.actamat.2009.12.013.
[73] J.-E. Brandenburg, L.A. Barrales-Mora, S. Tsurekawa, D.A. Molodov, Dynamic behavior of grain boundaries with misorientations in the vicinity of Σ3 coherent and incoherent twin boundaries in Al bicrystals, Acta Mater. 259 (2023), https://doi.org/10.1016/j.actamat.2023.119272.
[74] S. Mahajan, C.S. Pande, M.A. Imam, B.B. Rath, Formation of annealing twins in f.c.c. crystals, Acta Mater. 45 (1997) 2633–2638, https://doi.org/10.1016/S1359-6454(96)00336-9.